FACULTY OF ENGINEERING

Master Thesis

Investigation of Bismuth-Induced Surface Structures on InSb

Sina Ritter

29 August 2024

Supervisor: Prof. Rainer Timm
Assistant-supervisor: Rohit Yadav
Examiner: Assoc. Prof. Carina Fasth

Abstract

The investigation of Bismuth surface structures on InSb(110) surfaces is driven by the need to advance semiconductor technology for enhanced electronic device performance and new applications in optoelectronics and quantum computing. III-V semiconductors offer superior electronic properties compared to silicon. Incorporating Bismuth into these materials can significantly manipulate the bandgap, making them suitable for long-wavelength optoelectronic applications, and theoretical studies promise for these materials to behave as topological insulators with nearly lossless electron transport.

In this study, the evaporation and incorporation of Bismuth on InSb(110) surfaces is explored, focusing on the surface interactions and bonding states for bismuth evaporation at elevated sample temperature or at room temperature with subsequent annealing. Scanning Tunneling Microscopy (STM) is used to analyse the surface structure and X-ray Photoelectron Spectroscopy (XPS) to determine the chemical composition and bonding. Thereby, the STM studies show a local difference in the surface step density of the pure InSb surface. A higher step density is observed at the centre of the sample than at the edge, which is tied to an inhomogeneous distribution of strain during the sample cleavage or an inhomogeneous temperature distribution on the sample surface. The observed bismuth structures largely follow the underlying III-V lattice structure with a 1x2 reconstruction over large areas. However, bismuth islands independent of the substrate lattice are observed on the areas with a higher surface step density. During deposition at room temperature with subsequent annealing in a temperature range comparable to that of the STM sample, a 1x3 reconstruction was observed. The same was found with a sample that was heated during deposition to lower temperatures for a longer period of time. XPS data of the last two samples mentioned also show a difference in the types and amounts of Bi bonds. Thus, for subsequent annealing after deposition at room temperature, an increased amount of In-Bi bonds with respect to the Sb-Bi bonds are found, in comparison to the sample with deposition at elevated sample temperatures. Additionally, a higher stability of the amount of Bi on the surfaces under continued heating was observed in comparison to Bi deposition on a heated sample.

Consequently, it is discovered that the order of the treatment steps subsequently influences the type and amount of Bi bondings and the observed surface structure.

Making New Materials:

A Thin Layer of Bismuth atoms on a Semiconductor Substrate

Semiconductors, crucial materials that lie between insulators and metals, play a vital role in all electronic devices. With the miniaturisation of electronic components, the importance of surfaces, interfaces, and thin layers has grown.

III-V semiconductors, composed of elements from the third and fifth groups of the periodic table, are of particular interest as they are used in everyday electronics and also in many specialised products. Recent research has shown that incorporating bismuth into these semiconductors can significantly alter their properties. Bismuth can efficiently modify the material's bandgap, a central property of semiconductors. This bandgap also influences the optical properties, such as the colour of light emitted by an LED or laser made out of this semiconductors.

A thin bismuth layer on semiconductors like indium antimonide (InSb) is expected to exhibit unique electronic properties. These include the potential for spintronic applications, where electrons are separated by a quantum mechanical property called spin, and the formation of so-called topological insulators. These are materials that allow nearly lossless current flow, reducing device heating and energy consumption.

When bismuth is deposited on the semiconductor, it can form bonds with itself and with the underlying atoms. These bonds significantly influence the material's properties and the potential for forming a topological insulator. Theoretical studies suggest that bonds between bismuth and indium are promising for topological insulators.

In this study, Scanning Tunnelling Microscopy (STM) and X-ray Photoelectron Spectroscopy (XPS) are used to investigate the properties of bismuth on the semiconductor, comparing deposition on heated samples and room temperature samples which are subjected to post-deposition heating.

STM provides atomically resolved images of the sample's surface, revealing its topography, enabling us to observe where the bismuth atoms are located on the semiconductor surface. This technique showed different bismuth formations on the surface within individual samples and between different treatment methods.

XPS complements STM by ejecting electrons from atoms in the sample and measuring their energy. The energy depends on the chemical environment and bonding of the atom. By analysing the energy of the ejected electrons, we can infer the bonding nature of the atoms. This study observed that heat treatments increase the number of In-Bi bonds, which are crucial for the desired electronic properties.

Contents

1 Introduction

Technology and electronic components made from semiconductors are now ubiquitous in every aspect of life. As technology advances, more semiconductor components are being integrated into increasingly smaller spaces, enabling high-tech devices like smartphones to deliver the performance we expect (see Figure 1.1 for the development of the number of transistors on integrated circuits).[2]

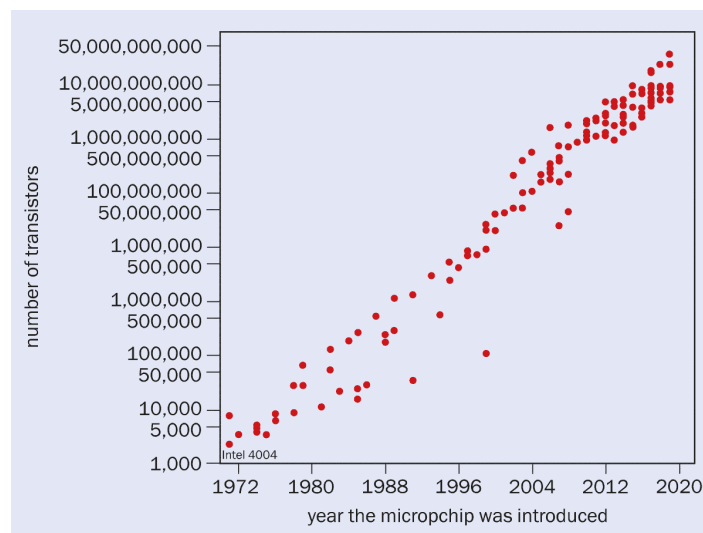Figure 1.1: Transistor density on integrated circuits per year. The density increases with an exponential growth, following Moor's law. Adapted from[15].

Due to the miniaturisation and densification of semiconductor-based technology, the surface and interface of adjacent materials have gained significant importance.[1] Consequently, there is now an increased interest in studying and understanding semiconductor surfaces and interfaces. Among the most promising material classes are III-V semiconductors, which exhibit superior electronic properties compared to the conventional semiconductor material silicon, such as higher charge carrier mobility and a direct band gap.[16] Moreover, combining various semiconductors from the third and fifth groups and varying their ratios can further influence and control properties like the bandgap, leading to different electronic and optical properties of the material. For example, a change in the bandgap of photo-luminescent semiconductors causes the emittance of light in a different colour than with the original bandgap.[8;9]

The integration of bismuth into III-V semiconductors has garnered significant interest recently due to its exciting possibilities for bandgap manipulation, especially in semiconductors with a narrow bandgap like InSb. Partially replacing the group V elements with Bi in any III-V alloy reduces the bandgap, making Bi-containing alloys suitable for applications in optoelectronics, particularly in the long wavelength regimes.[8;9] This

bandgap reduction is attributed to Bi's status as the largest naturally occurring group V element and its correspondingly lower electronegativity compared to other elements in the group.

One approach involves partially or completely replacing group-V atoms with Bi within the crystal lattice during bulk growth. However, achieving high concentrations of Bi in bulk-grown alloys is challenging, with the Bi concentration not exceeding 20% of the group-V atoms so far.[9;17;18] Another approach entails Bi deposition onto a III-V substrate, yielding either free-standing 1D chains, 2D or 3D III-V layers with increased Bi content or metallic Bi islands for larger Bi depositions.[19;10] While metallic Bi layers show promise in various applications, such as energy storage devices, and are widely investigated, the interface between metallic Bi and the III-V substrate remains largely unexplored. This is despite contact issues, causing loss in electronic performances of devices at these interfaces.[20;21]

In this study, the focus is on the evaporation and incorporation of bismuth on the (110) surface of InSb to create one- or two-dimensional bismuth structures. These bismuth structures on InSb have emerged in theoretical studies as promising candidates for topological insulators, materials exhibiting non-trivial topological properties, leading to stable conducting boundary states while maintaining an insulating interior. Protected by the material's topology, these conducting boundary states offer nearly lossless electron transport with a fixed relationship between momentum and spin, enabling applications in electronics, quantum computing, and spintronics.[10–13]

Among these materials, InBi is particularly intriguing due to its significant spin-orbit coupling, which theoretically results in an inverted bandgap large enough to enable quantum applications at room temperature. This unique property positions InBi as a promising candidate for advancing next-generation electronic and quantum devices.[11;14]

Previous investigations on the deposition of Bi onto polar InSb(111) surfaces have predominantly shown Sb-Bi bonds.[22] However, the study of Bi on non-polar III-V alloy surfaces like InAs(110) has shown an increased number of In-Bi bonds at elevated sample temperatures during deposition, which raises the interest in studying the evaporation of Bi under different conditions.[23]

This work concentrates on the non-polar InSb(110) surface and investigates the evaporation of Bi at both elevated sample surface temperature and room temperature with subsequent annealing. First, the structure of the clean InSb(110) surfaces is studied with scanning tunneling microscopy (STM). Then, since an higher number of In-Bi bonds are expected, the results of Bi deposition at elevated sample temperatures is investigated with STM, showing Bi-induced surface structures. Fast Fourier transformation (FFT) is applied to the STM images, transforming the image into the Frequency space, revealing periodicities and the corresponding frequencies. The chemical composition and the bonding of the Bi onto the substrate is then studied with X-ray photoelectron spectroscopy (XPS). Since the STM and XPS measurements could not be conducted on the same sample, due to limitations in the measurement setups, LEED measurements are used to identify surface structures of the XPS sample and to revise if the XPS and STM sample are similar. A second approach with deposition at room temperature with subsequent annealing is also undertaken for a comparison of these different approaches. Again, STM, XPS and LEED studies are conducted.

2 Theoretical Background

2.1 Scanning Tunneling Microscopy

STM is a technique to image the topography and electronic properties of a conducting surface with atomic resolution, by using a tunneling current between a metallic tip and a conductive sample. The tip is kept in a close proximity to the sample and scanned over an area of up to a few hundred micrometer squared. Thereby, the tip does not touch the sample, but a tunneling current between tip and sample can be measured. Either the variance in tunneling current or the change in tip-sample distance to obtain a constant tunneling current can be used to acquire an image of the sample surface. This method enables the visualisation of the topography and the local density of states at a sample surface, which contributes to the understanding of surface and electronic properties of materials at the atomic level.

The principle of STM is rooted in quantum mechanical tunneling. A particle like an electron can quantum mechanically tunnel through a potential barrier of height Φ, which the particle could not overcome classically.[24;25]

Thereby, the wave function of the particle decays exponentially inside the barrier, which is given in Equation 2.1 in the one-dimensional case.[24]

$$\Psi(x) = \Psi(0)e^{-x/\hbar\sqrt{2m(\Phi-E)}} \tag{2.1}$$

Here, Ψ is the wave function of the particle, x is the distance covered in the potential barrier, Φ is the height of the potential barrier, m is the mass of the tunneling particle, $\hbar$ is the reduced Planck constant and E is the energy of the particle.

This leads to a tunneling intensity:

$$T = \frac{|\Psi(d)|^2}{|\Psi(0)|^2} = e^{-2d/\hbar\sqrt{2m(\Phi-E)}} \tag{2.2}$$

where d is the width of the barrier.[5]

In the case of STM, the vacuum gap between the metallic STM tip and the conductive sample presents a potential barrier. This barrier's height is determined by the difference between the Fermi level E_F of the material and the vacuum level E_{vac}, also known as the work function Φ of the material. An electron can tunnel through this barrier, if the barrier is small enough.[24;25]

A tunneling current can only occur, if there are empty states on one side, which can be occupied by electrons tunneling through the barrier from the other side (sample to tip or tip to sample). Since in equilibrium, the Fermi levels of tip and sample are equal there is no free states available for tunneling and no net charge transfer. Therefore, a bias voltage V_B has to be applied to offset the Fermi energies of the sample and the tip.[25]

Figure 2.1 depicts the energy digrams for a semiconducting sample and a metallic tip without bias and with negative and positive sample bias, respectively. Depending on the bias, electrons tunnel from the sample to the tip (negative sample bias) or from the tip to the sample (positive sample bias).
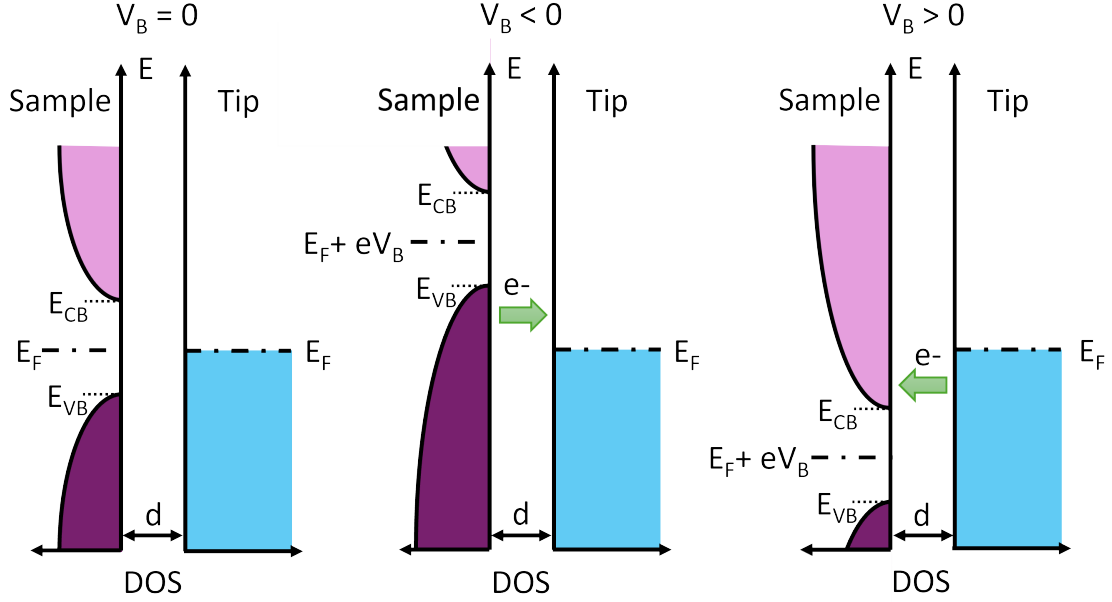

Figure 2.1: Energy diagram of a semiconducting sample and a metallic tip with a distance d between them with different sample biases, while the tip is grounded. Electrons tunnel from the sample/tip to the tip/sample for a negative/positive sample bias.

According to Fermi's golden rule, the transition probability Γ_{i-f} from the initial state i before tunneling to a final state f where an electron tunnelled elastically through the barrier is given by Equation 2.3.

$$\Gamma_{i-f} = \frac{2\pi}{\hbar}|M|^2 \tag{2.3}$$

where M is the matrix element of the transition.[26]

Bardeen derived an Equation for the tunneling current (see Equation 2.4), based on Fermi's golden rule and assumptions, such as the independence of the tip and sample wave functions from each other and from the tunneling process.[27]

$$I_t = \frac{4\pi e}{\hbar} \int_{-\inf}^{\inf} \rho_S(\epsilon + eV_B)f_S(\epsilon + eV_B)|M|^2\rho_T(\epsilon)[1 - f_T(\epsilon)]d\epsilon \tag{2.4}$$

with the Fermi function

$$f(E) = \frac{1}{1 + e^{(E-E_F)/k_B T}} \tag{2.5}$$

Here, $\rho_S(E)$,$\rho_T(E)$ give the density of states at the energy E within the sample or tip respectively. The Fermi function $f(E,T)$ gives the probability of the occupation of an energy state E at a temperature T. e denotes the elemental charge of an electron. The Fermi energy E_F is set to zero. Consequently, Equation 2.4 gives the tunneling current

for tunneling from occupied states in the sample, biased with V_B, to an unoccupied state in the unbiased tip.

Tersoff and Hamann simplified this expression with the assumption of an s-type wave function for the tip, with a constant ρ_T and the assumption of low temperatures, leading to step-like Fermi functions.[28] This leads to the simplified Equation 2.6 for the tunneling current.

$$I_t = \frac{4\pi e}{\hbar} \rho_T \int_{E_F - eV_B}^{E_F} \rho_S(\epsilon + eV_B)|M|^2 d\epsilon \tag{2.6}$$

With Tersoff's and Hamann's approximations, the matrix element M is proportional to the tunneling intensity T given in Equation 2.2, i.e. the tunneling current is exponentially proportional to the distance between the tip and the sample. Consequently, the measured tunneling current for a constant distance between sample and tip reflects the local density of states of the sample integrated over all energy states between $E_F - eV$ and E_F.

Tersoff's and Hamann's approximation of low temperatures is usually applicable for semiconductors, where $k_B T <$ Band gap. The assumption of a constant density of states of the tip, however, is often not realistic, since real tip shapes usually deviate form the ideal one. Consequently, the observed current is a result of the convolution of the density of states of tip and sample.

2.2 X-ray Photoelectron Spectroscopy

X-ray photoelectron spectroscopy (XPS) is a method which is complementary to STM. While also being a highly surface sensitive technique, XPS gives insights on the chemical composition and chemical bondings present on the sample surface. Different bondings between surface atoms result in a different signal in the XP (X-ray photoelectron) spectra. By identifying the location of different types of bonding in the spectra and comparing the intensity of the individual spectral peaks, the types of bondings and their relative quantities can be assessed. These, in turn, determine the surface properties and electronic properties of the sample.[29–31]

X-ray photoelectron spectroscopy (XPS) refers to the measurement of the energy distribution of electrons emitted from a material due to the photoelectric effect by the radiation with X-rays.

Hereby, X-rays refers to electromagnetic radiation with the wavelengths in the range of 0.1 Å to 100 Å, which corresponds to a photon energy of approximately 100 eV to 100 keV.[5]

The generation of these X-rays will be discussed in Section 3.2.1.

To emit an electron, the binding energy E_{BE} of the electron in the atomic lattice as well as the work function of the material Φ_S have to be overcome, leaving the remaining energy of the radiating light for the kinetic energy of the emitted electron.[29] Hereby, the binding energy E_{BE} is defined as the energy difference between the Fermi level and the specific energy level of the electron within the atomic lattice, i.e. the energy of the core levels they are situated in. The work function Φ_S is then the minimum energy needed to

remove an electron from the solid, i.e. the difference between the Fermi level and the vacuum level.

$$h\nu = E_{BE} + E_{kin} + \Phi_S \tag{2.7}$$

where $h\nu$ is the energy of the incoming light. The electrons can be detected by a spectrometer, which resolves their kinetic energy. Since the work function of the spectrometer can differ from the material work function, the detected kinetic energy depends on the spectrometer's work function, which is also illustrated in Figure 2.2.[32;33] The detected kinetic energy is therefore given by Equation 2.8

$$E_{kin,det} = h\nu - E_{BE} - \Phi_{Spec} \tag{2.8}$$

Since the photon energy $h\nu$ and the work function Φ_{spec} are known and E_{kin} is measured, the binding energy of the electron can be determined.[32;33]
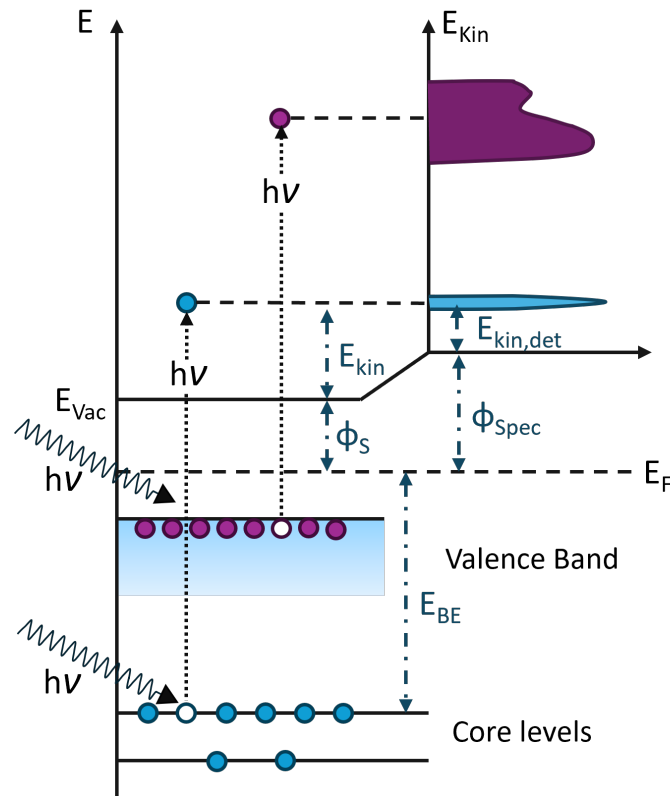
Figure 2.2: XPS energy diagram. Electrons from core levels with binding energy E_{BE} (blue) and electrons from the valence band (purple) are excited by incoming electromagnetic radiation with energy $h\nu$ resulting in an XPS spectrum shown to the right. The peaks of the valence band electrons are significantly broader than from the core level due to the energy broadness of the valence band. The detected kinetic energy $E_{Kin,det}$ differs by $\Phi_{Spec} - \Phi_S$ from the actual kinetic energy of the electrons. Inspired from[5].

The emitted electron can originate from the valence band, i.e. from a continuous energy band, or from discrete core levels. Due to their continues range of binding energies, valence electrons result in a broad peak in the XPS spectrum, while core electrons result

in sharp peaks at discrete energies, corresponding to Equation 2.8. By using light in the X-ray regime, the photon energy is in a similar energy range as the binding energy of the core electrons, resulting in mainly measuring core electrons. Since core electrons emitted form within the sample can experience inelastic scattering during their way to the sample surface, a distribution of detected E_{kin} creates a background underlying the core level peaks.[29]

The mean distance an electron can travel before undergoing inelastic scattering is described by the inelastic mean free path of electrons. It defines the depth from which the electrons can escape the surface of the sample without losing energy and is a property dependent on the electron's kinetic energy (see Figure 2.3). By choosing a photon energy corresponding to a kinetic energy of around 10 to 150 eV, only electrons from the outer most atomic layers can escape the surfaces and are detected, which corresponds to a highly surface sensitive measurement.[4;33;34]
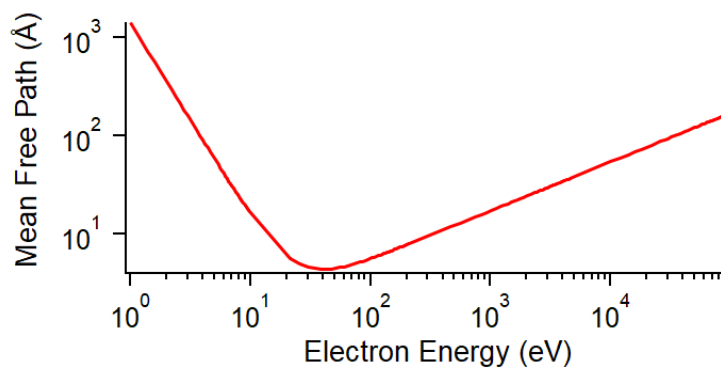

Figure 2.3: The so called universal curve, showing the inelastic mean free path of electrons in respect to their kinetic energy. Plot based on Equations from[35]
.

Since the probability of electron emission from a certain energy state depends on the density of electrons available at this state, the number of detected electrons at a certain binding energy correlates to the density of states at this energy.[29]

2.3 LEED

Low energy electron diffraction (LEED) is a technique to analyse the long-range surface structure of crystalline samples. In contrast to STM, LEED gives information about periodic surface structures over a bigger surface-area (a few square millimetres) of the sample. In this technique, the surface of a crystalline sample is bombarded with a collimated electron beam with an electron energy in the range of about $20 - 500$ eV. In this energy range, the inelastic mean free path of the electrons is in the order of a few Ångström, corresponding to a few atomic layers, leading to the high surface sensitivity of the technique. The incident electrons are scattered at the periodic atomic arrangement at the crystalline sample surface and undergo diffraction. Inelastically scattered electrons are suppressed by hemispherical grids, while the elastically scattered/diffracted electrons are then detected by a usually hemispherical phosphor screen (see Figure 2.4 (a)). A

projection of the diffraction pattern is then visible on the screen. For a periodic surface structure, this diffraction pattern corresponds to the two-dimensional surface reciprocal lattice, giving information about the atomic arrangement on the sample surface. An example of such a LEED pattern is given in Figure 2.4 (b).[36]
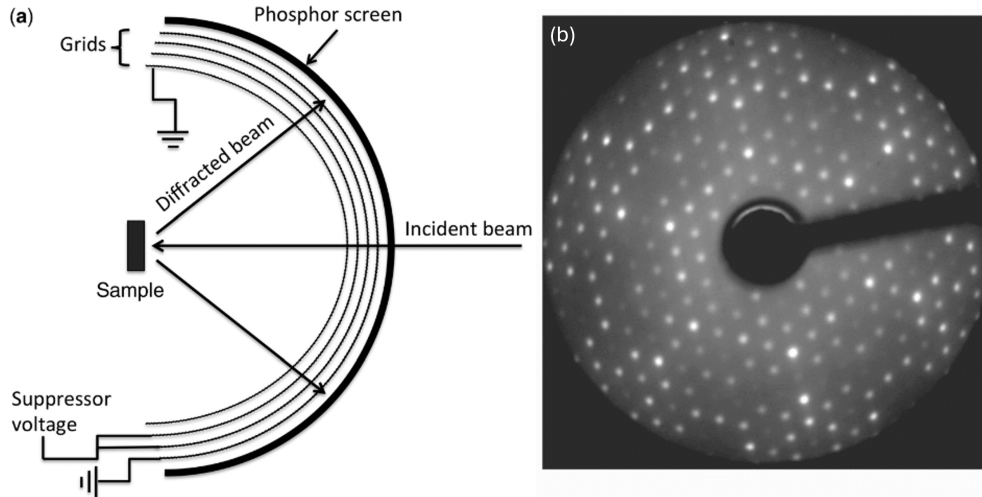

Figure 2.4: (a) Geometry of a hemispherical LEED. (b) LEED pattern from the 6x6 structure of $Al(111)$-$(6x6)$-$3C_{60}$ using a hemispherical LEED. Adapted from[36].

2.4 Surface Reconstruction

When observing a sample's surface, the view differs from what is seen within the bulk. At the surface of the sample, the symmetry of the bulk is broken and the surface atoms are missing bonding partners, resulting in dangling bonds. To decrease the number of dangling bonds and to minimize the surface energy, the surface atoms can either relax, i.e. change their distance to the underlying layers in respect to the bulk, or reconstruct, i.e. rearrange in a 2D matter and form different bondings among them. For Semiconductors, surface reconstructions are common. The absorption of ad-atoms onto the sample can also cause a reconstruction or a change in the overlaying reconstruction.[37][38]

2.4.1 Wood's Notation

To describe the overlaying surface structure, the Wood's notation is introduced. The overlying structure and the underlying atomic layer are described by the vectors $T_A = na_1 + ma_2$ and $T_B = nb_1 + mb_2$ respectively (see Figure 2.5 (a) for an example where blue circles represent the overlying structure). In the Wood notation, the ratios between a_1 to b_1 and a_2 to b_2 are considered, as well as a possible rotation by an angle Φ between the two layers:

$$\left(\frac{b_1}{a_1} x \frac{b_2}{a_2}\right) R\Phi \qquad (2.9)$$

Furthermore, the surface under consideration can be specified in the form of its Miller indices $\{hkl\}$, the substrate M and, in the case of an adsorbate A, this too:

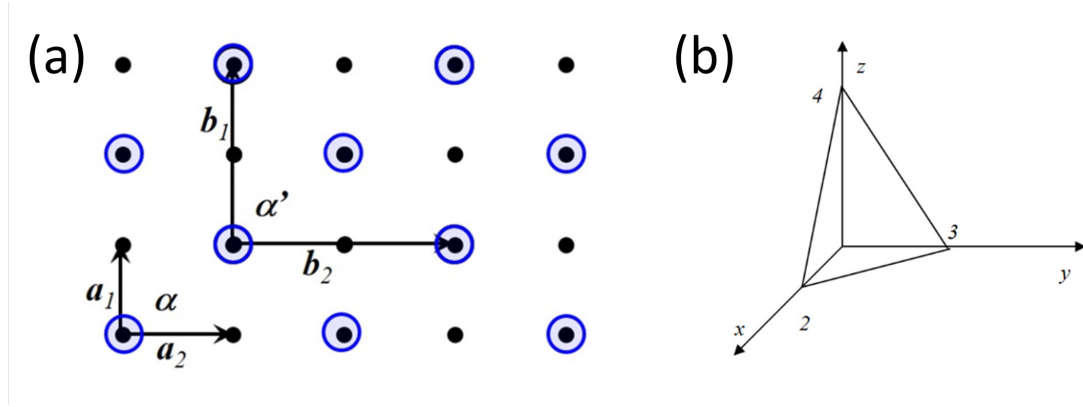$$M\{hkl\}\left(\frac{b_1}{a_1} x \frac{b_2}{a_2}\right)R\Phi - A \tag{2.10}$$

Figure 2.5: (a) Schematic top-view of a reconstruction on a substrate surface. Substrate atoms are shown as black dots and the overlaying atoms are shown as blue circles. a_1, a_2, b_1, b_2 are the vectors to describe the surface structures and α and α' are the angles between the related vectors. (b) Example of a plane for Miller indexing. The Miller index is (643). Adapted from [38]

For an angle of $\Phi = 90°$ and well known substrate and sample, it is possible to only state the ratios $\frac{b_1}{a_1} x \frac{b_2}{a_2}$.

The Miller indices are a way of identifying a plane or a direction in a crystal. The intersection points of the plane with the lattice vectors of the unit cell of the three-dimensional crystal, c_1, c_2, c_3, are determined and their reciprocal value is multiplied by a factor so that all three values correspond to integers. If the plane has no intersection with a Lattice vector, the Miller index is 0. An example of a plane and the determined Miller indices is given in Figure 2.5 (b). The plane intersects the axes at $c_1 = 2$, $c_3 = 3$ and $c_4 = 4$, resulting in the Miller indices $(\frac{12}{2}, \frac{12}{3}, \frac{12}{4}) = (6, 4, 3)$.[38]

2.5 Indium Antimonide (InSb)

InSb is the III-V compound semiconductor with the smallest bandgap (approx 0.18 eV at 300 K) and biggest lattice constant ($a_0 = 6.48$ Å).[39;40] It has a zinkblende structure, which consists of two FCC lattices, one for each element, which are shifted by $(\frac{1}{4}, \frac{1}{4}, \frac{1}{4})$ of the three-dimensional unit cell in respect to each other.[41] The crystal structure is shown in Figure 2.6 (a). In this work, the (110) surfaces of InSb will be investigated. These consists of zick-zack lines of alternating Sb and In atoms, which can also be seen as two close lines of Sb and In respectively. The (110) plane in the unit cell is shown in Figure 2.6 (a) and a top view of the (110) plane is shown in Figure 2.6 (b).
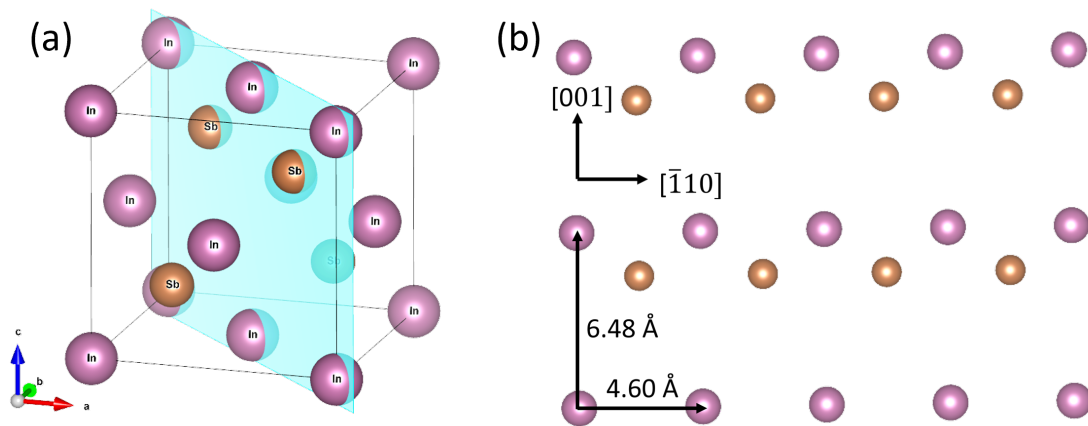
Figure 2.6: Zinkblende crystal structure of InSb. (a) unit cell of InSb with (110) plane in cyan, In atoms in purple and Sb atoms in brown. (b) Top-view of the (110) plane of InSb. Figures created with VESTA.[42]

3 Experimental Methods

3.1 STM Setup Idefix

Most of the STM measurements conducted in this work were performed using the in-house ultra-high vacuum (UHV) system, shown in Figure 3.1. Samples can be introduced into the UHV system via the loadlock. The deposition of bismuth was conducted in the preparation chamber. The evaporator is positioned at the bottom, oriented at a $45°$ angle to the horizontal, and is located in a distance of approximately 10 cm from the sample. The sample holder can be heated using the manipulator, with the actual temperature on the (110) surface of the sample being monitored by a pyrometer. STM measurements are conducted in the analysis chamber, which maintains an operating pressure between 10^{-11} and 10^{-10} mbar with an Omicron VT-STM.

(a) UHV setup   (b) STM setup
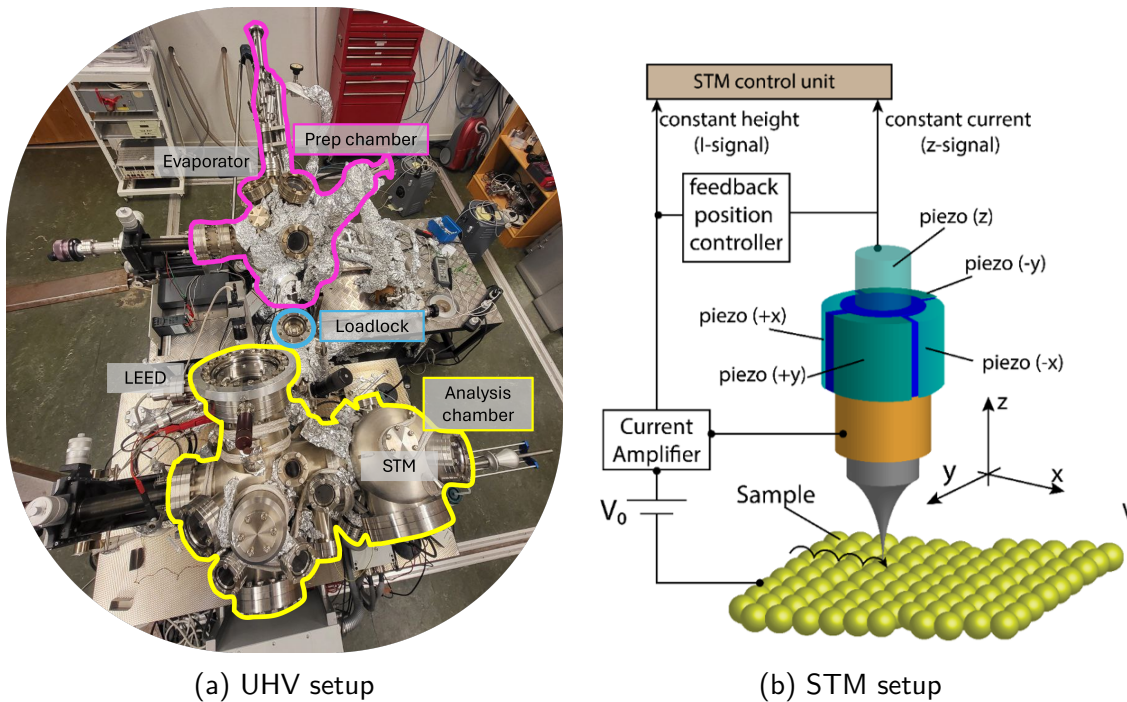
Figure 3.1: (a) Top-view of the UHV setup used for STM measurements. Bismuth is deposited on the sample in the preparation chamber. Cleaving of the sample, necessary to access the (110) surface, as well as STM measurements are executed in the analysis chamber. The marked LEED was added after the measurements of this work were finished. (b) Sketch of the STM setup. Piezo actuators are used for the tip movement. In constant current mode, a feedback loop is used to adjust the z-position accordingly. The used STM is upside down, i.e. the sample is above the tip and the tip looks upwards. Adapted from reference[43].

The basic setup of an STM is shown in Figure 3.1b. During operation, the STM tip, typically made of etched tungsten wire, is positioned approximately 1 nm from the sample surface. This minimal distance, combined with the exponential relationship between the tunneling current and the tip-sample distance, necessitates effective damping of the system against external vibrations and precise control of the STM tip position. The tip is controlled by coarse motors and piezo actuators, which offer sub-angstrom accuracy, thereby enabling atomic resolution.

For the measurements conducted in this study, the STM was operated in constant current mode. In this mode, the tunneling current is kept constant while the height of the STM tip is adjusted through a feedback loop.

3.2 XPS Measurements at Max IV

The XPS measurements in this work were executed at the EA01 endstation at FlexPES (Flexible PhotoElectron Spectroscopy) and the ARPES (Angle Resolved PhotoEmission Spectroscopy) endstation at BLOCH, which are both beamlines at the 1.5 GeV storage ring of the MAX IV Laboratory, Sweden.

3.2.1 X-ray Generation

Synchrotron radiation, first emerging in the 1960s, is generated by the acceleration of electrons in a magnetic field. After the electron beam is generated in an electron gun, the electrons are accelerated to near-light speeds in a storage ring. In this ring, the electrons travel in a vacuum along a polygonal path composed of straight segments and bends. Bending magnets direct the electrons onto curved paths, causing them to emit synchrotron radiation.[44] By implementing periodic arrays of magnets with alternating polarity, synchrotron radiation with lower divergence can be generated than by the bending magnets. These arrays, known as insertion devices, cause the electrons to "wiggle" and emit radiation in the forward direction. The insertion devices are divided into wigglers and undulators, which differ in magnetic field strength and the spacing between the magnets.[44] At MAX IV, undulators are used, which, compared to wigglers, have smaller magnetic fields and thus cause smaller electron deviations.[44;45] Through constructive interference, X-rays with a narrow energy range are produced. Compared to X-ray tubes, which preceded synchrotron sources and are still used in laboratories, synchrotron sources offer monochromatic and broadband radiation with tunable energy over a wide range, from infrared to hard X-rays exceeding 100 keV. They provide significantly higher photon flux and can focus X-rays down to nanometre-scale spots, making them ideal for detailed studies of the atomic structure and chemistry of materials.[44]

3.2.2 Detection of Photoelectrons

The photoelectrons, generated after the X-ray-sample interaction, reach an hemispherical analyser (Sketch in Figure 3.2). There, a voltage is applied to the outer and inner sphere causing the bending of the beam of electrons. Only electrons within a certain range of energies, defined by the pass energy, reach the detector at the end of the analyser.
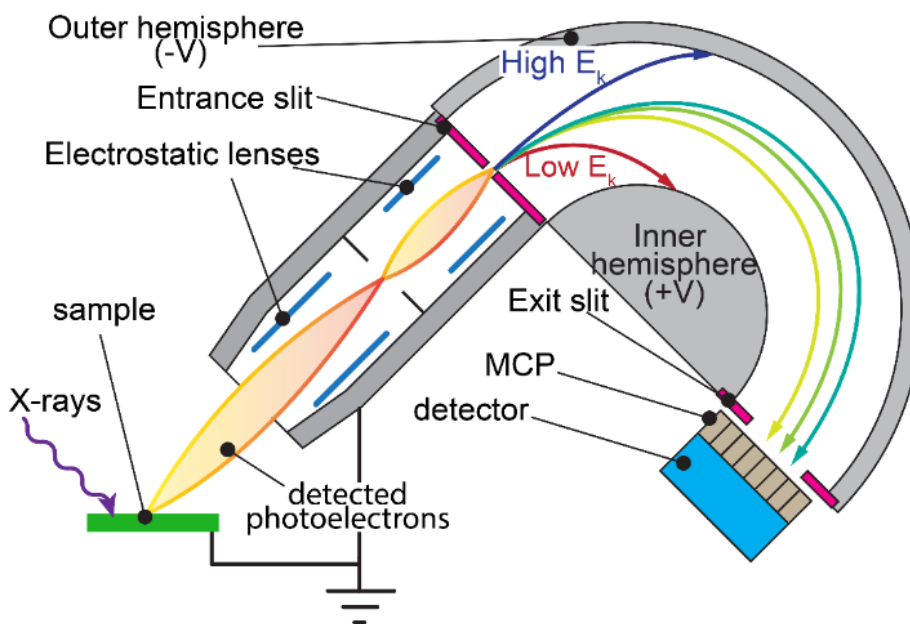
Figure 3.2: XPS setup with electrostatic lenses to focus the photoelectrons, a hemispherical analyser with biased inner and outer walls, the micro channel plate for electron multiplication and the detector. Adapted from[43]

3.2.3 FlexPES Beamline Max IV

FlexPES allows X-ray radiation with a photon energy in the range from 40 to 1500 eV and is a beamline specialized for high-resolution photoelectron spectroscopy in UHV.[46] The setup is shown in Figure 3.3. XPS measurements were executed in the experimental chamber. Bismuth evaporation was done in the second preparation chamber. Thereby, the evaporator was facing from below towards the sample surfaces with an approximate angle of $45°$ to the horizontal and a distance of approximately 10 to 15 cm from the sample. The sample heating was done with a hot filament. Since the used sample holder did not have contacts for a thermocouple and the sample surface was not visually accessible, the actual temperature on the sample surface had to be estimated with reference measurements on a regular metal plate sample holder without sample. LEED measurements were executable in the main preparation chamber. The operating pressure during XPS never exceeded 10^{-10} mbar.

3.2.4 BLOCH Beamline Max IV

Bloch is a beamline primarily for angle resolved photoemission spectroscopy (ARPES) in the low energy regime ($10-250$ eV), but can be operated with photon energies up to 1000 eV.[48] XPS measurements were executed in the analysis chamber, while sample heating and simultaneous LEED measurements were done in the preparation chamber marked in yellow in Figure 3.4. The bismuth evaporator was facing upwards with an approximated angle of $45°$ to the horizontal and a distance of approximately 10 to 15 cm from the sample. Additionally, the setup is equipped with an STM, enabling XPS and STM measurements on the same sample without leaving the UHV.
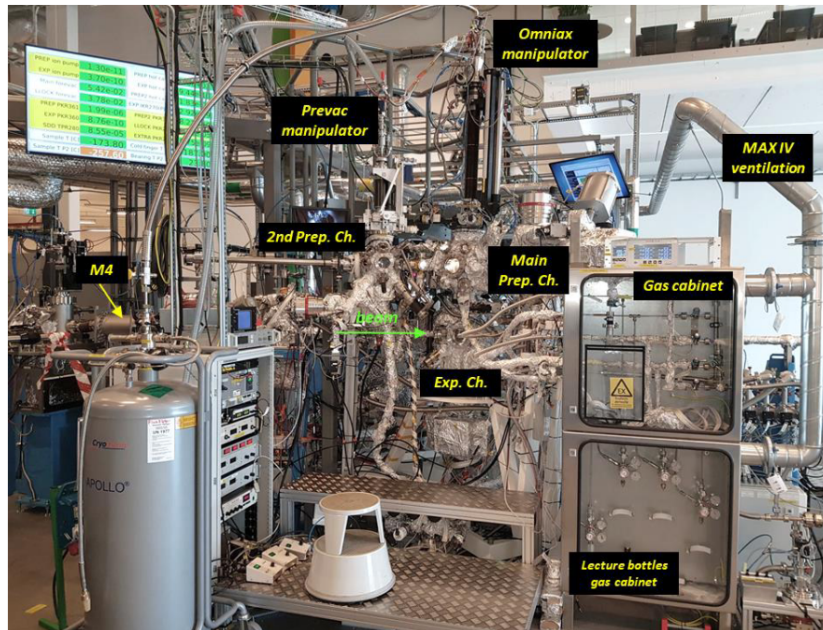
Figure 3.3: EA01 Endstation FlexPES. Bismuth evaporation is done in the 2nd preparation chamber. LEED measurements are done in main preparation chamber. XPS measurements are done in the Experimental chamber. Adapted from [47]
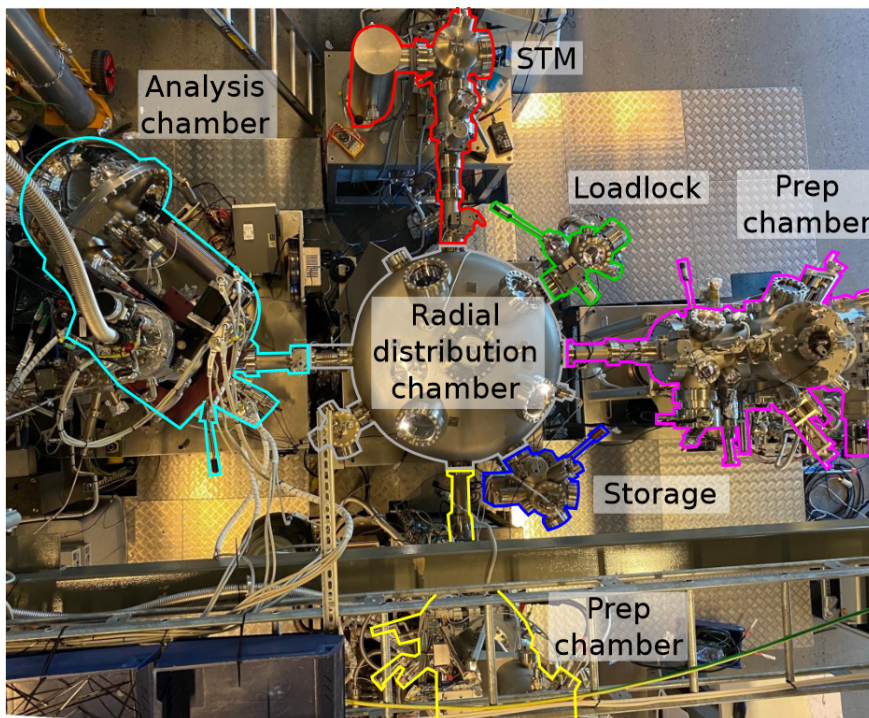
Figure 3.4: A-branch endstation BLOCH. Sample heating and LEED measurements were done in the preparation chamber marked in yellow. Through the Radial distribution chamber, the sample could be moved between the analysis chamber for XPS measurements, sample heating in the prep: chamber and STM measurements without leaving the UHV. Adapted from [48]

3.3 Analysis of XPS Data

When considering and analysing XPS core-level data, there are several aspects that need to be taken into account in order to draw physically meaningful conclusions. The interaction between spin and momentum, the so-called spin-orbital interaction, causes an electron configuration state with the same angular momentum L to split into two energy states, corresponding to the two associated total angular momentum quantum numbers J at a distance of the order of eV. This so-called spin-orbital splitting is visible in the XPS spectrum by two peaks, a doublet, which have a fixed energy distance from each other and have a fixed intensity ratio (see Figure 3.5). This intensity ratio, the branching ratio, arises from the different microstates to the respective total angular momentum quantum number. While a state with $J = 5/2$ has 6 microstates ($2*J + 1$), the state with $J = 3/2$ contains 4 microstates, which leads to a theoretical branching ratio of 6:4, i.e. 3:2. In reality, however, the branching ratio usually deviates from the theoretical value.[30;31] An example of an Au 4f spectrum is given in Figure 3.5, where the branching ratio and the spin-orbital splitting are indicate with blue arrows.

Figure 3.5: Spectrum of Au 4f taken with a photon energy of 340 eV. The spin-orbital splitting and the branching ratio are indicated with blue arrows.

The line shape of the peaks is composed of the natural linewidth due to the uncertainty principle and a broadening by instruments and other factors, whereby the former generates a Lorentzian energy distribution and the latter a Gaussian distribution. Therefore, the final peak line shape is a convolution of Gaussian and Lorentzian, the so-called Voigt function. The Lorentzian and Gaussian parts can vary and are determined by the Gaussian and Lorentzian full-width-half-maximum (FWHM) respectively.[30;31]

The energy at which the peaks occur is primarily determined by the core levels from which the photoelectron is excited. These core levels are associated with particular atoms, and the binding energies of the electrons to these atoms depend on the element of the atom. Thereby, each element causes peaks in the XPS data at specific energies. A determination if these peaks help to identify elements in the sample. The position of the peaks is also significantly influenced by the chemical and physical environment of the atoms form which the photoelectron is excited. Bonding partners and the general environment

of these atoms can affect the binding energies of the electrons. Photoelectrons originating from atoms with different bonding partners or environments can therefore exhibit different chemical shifts, resulting in the separation into different peaks, which can differ by up to a few eV. Therefore, with XPS data it is possible to determine different chemical states and the ratio of the number of atoms in these states.[30;31]

When analysing XPS data, special consideration must be given to the background of the measurements. This background comes mainly from the loss of energy of the electrons as they travel through the sample or gas and is higher for lower kinetic energies. A common method to model the background is the Shirley background. Here, the intensity of the background at a given binding energy is proportional to the total intensity of the spectrum from this binding energy up to higher energies. This creates a step-like background, which further increases with higher binding energy.[30;31]

4 Sample Preparation

4.1 Sample Cleavage

The sample was cut out of an InSb Te doped (100) wafer purchased from wafertech from the ingot with the number M8/699/Te. The (110) plane is the cross section of the (100) wafer and can be accessed by cleaving the (100) wafer. This technique is preferable over a (110) wafer, since the cleaving can be done in UHV, without exposing the (110) surface to ambient pressure. Thereby, the (110) surface stays relatively clean and no further cleaning of the surface is necessary. For the cleaving, a small cut was made with a diamond cutter on the sample as marked in Figure 4.1. In the UHV, pressure is applied to the side of the sample where the crack is located using a transfer arm or manipulator to initiate the cleavage of the sample.
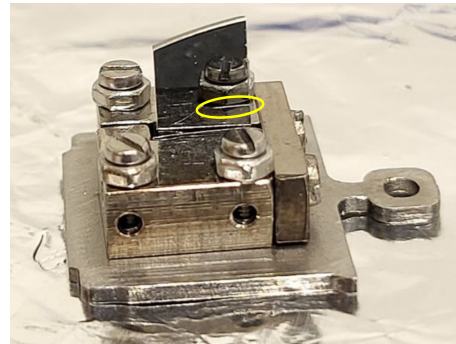

Figure 4.1: Non-cleaved InSb sample in a cross-sectional sample holder. A cut by a diamond cutter, marked with a yellow oval, sets the starting point for the sample cleavage to expose the (110) plane.

4.2 Bismuth Evaporation and Heat Treatment

For the Bi deposition, a low temperature effusion cell from MBE-Komponenten was used as illustrated in Figure 4.2. Here, solid Bi drops are inserted into the crucible, which is then heated by a tantalum wire filament, to melt and finally evaporate the Bi. The release of the gaseous Bi is controlled by a Te shutter plate to regulate the exposure of the sample to the Bi.

Different approaches are being tested to achieve stable bonds between the bismuth atoms and the semiconductor substrate. Therefore, various deposition processes were used, and their results are compared in this work. The sample used for the STM investigation and the sample examined at the FlesPEX beamline were heated during deposition, while the sample studied at the Bloch beamline was kept at room temperature during deposition and subsequently heated afterwards.

The different sample process steps for the three different samples are given in Table 4.1. Since the deposition of bismuth was done in different UHV chambers, the angle and the distance between the evaporator and the sample varied, which complicated the comparison between the different samples.

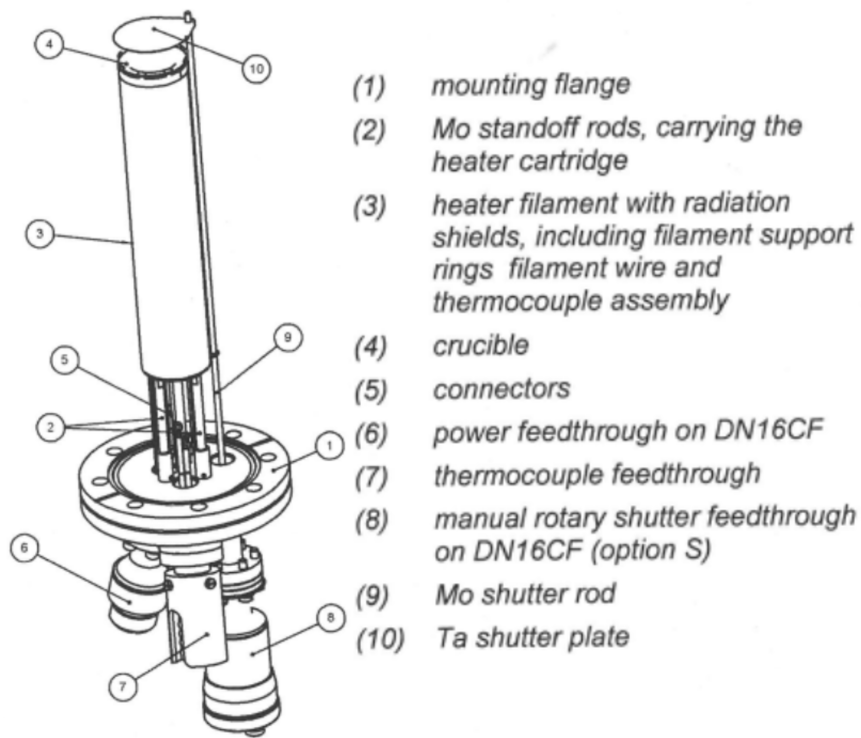|	
(1)	mounting flange
(2)	Mo standoff rods, carrying the heater cartridge
(3)	heater filament with radiation shields, including filament support rings filament wire and thermocouple assembly
(4)	crucible
(5)	connectors
(6)	power feedthrough on DN16CF
(7)	thermocouple feedthrough
(8)	manual rotary shutter feedthrough on DN16CF (option S)
(9)	Mo shutter rod
(10)	Ta shutter plate

Figure 4.2: Illustration of the low temperature effusion cell used for Bi deposition. The initially solid Bi is inserted into the crucible and heated by a Ta filament till evaporation. Adapted from [49].

Furthermore, monitoring and measuring the temperature on the sample surface during annealing and deposition is challenging, as a thermocouple cannot be attached to the sample holder used. Additionally, the sample holder has a significantly greater mass than conventional flat sample holders, which can make comparisons with reference measurements inaccurate. The protrusion of the sample from the sample holder also contributes to potentially inhomogeneous heating of the sample.

The temperature readings from FlexPES were extrapolated using a reference measurement on an empty conventional sample holder, which, as described above, can yield significantly higher temperature values than those actually present on the sample surface.

In Bloch, the temperature was determined directly from the heating system below the sample holder, which is associated with similar inaccuracies as for FlexPES.

In the STM measurements, a pyrometer was used to directly determine the temperature on the sample surface. Here, the measurement range of the pyrometer is larger than the sample surface, which can lead to deviations. However, these deviations should be significantly lower than those of the other methods used.

Table 4.1: Preparation step of the different samples investigated in this work. The temperatures for the FlexPES sample are extrapolated from a measurement on an empty sample holder. The temperature at Bloch is not for the sample surface but for the bottom of the sample holder. T_{Evap} stands for the temperature of the filament in the evaporator during Bi evaporation, T_S is the measured temperature of the sample, t is the duration of the respective treatment. $t_{sampleheating}$ refers to an additional timespan of sample heating prior to evaporation.

STM studies	FlexPES	BLOCH
Sample annealing $T_S = 300°C$ $t = 15$ min	**1st Bi deposition** $T_S \approx 250°C$ $T_{Evap} = 418°C$ $t_{sampleheating} \approx 20$ min $t = 5$ min	**1st Bi deposition** $T_S = RT$ $T_{Evap} = 445°C$ $t = 5$ min
Bi deposition $T_S = 250°C$ $T_{Evap} = 466°C$ $t = 10$ min	**2nd Bi deposition** $T_S \approx 250°C$ $T_{Evap} = 457°C$ $t_{sampleheating} \approx 20$ min $t = 5$ min	**Sample annealing 0.1** $T_S = 200°C$
	3rd Bi deposition $T_S \approx 250°C$ $T_{Evap} = 453°C$ $t_{sampleheating} \approx 1.5$ h $t = 10$ min	**2nd Bi deposition** $T_S = RT$ $T_{Evap} = 445°C$ $t = 7$ min
		1st sample annealing $T_S = 258°C$
		2nd sample annealing $T_S = 256°C$ $t = 2$ h
		3rd sample annealing $T_{S,max} = 350°C$ $t = 4$ h T increased over time, t is total annealing time
		4th sample annealing $T_S > 400°C$ $t = 5.6$ h T increased over time, t is total annealing time

5 Results

5.1 STM Analysis of the Clean InSb Surface

At the beginning, the clean InSb(110) surface was analysed using STM. STM images were taken with a negative tunneling voltage. The chosen negative voltage allows for a more stable STM tip, resulting in better STM images than with a positive voltage. However, in this settings, only the filled states, which are located at the antimony atoms, are observed.
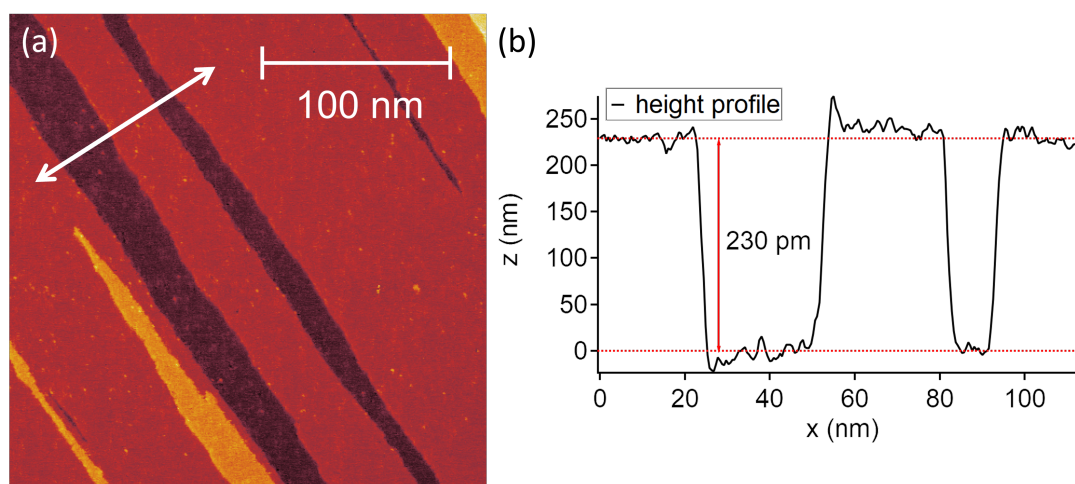

Figure 5.1: (a) STM images from the clean InSb (110) surface taken at the edge of the sample. The position on the sample, where the image was acquired is indicated with a cross on the sketch to the right. (b) Height profile taken along the white arrow in (a). $V = -2.5$ V, $I = 100$ pA.

Figure 5.1 shows an image of the clean InSb(110) surface. The surface is flat with isolated steps. A height profile, taken along the white arrow in Figure 5.1 (a), is shown in Figure 5.1 (b). The terrace height was determined to be 230 ± 5 pm, which was confirmed by measurements on additional STM images not included in this work.

This value corresponds to the height of a monolayer in the (110) plane, as illustrated in Figure 5.2. The distance between two antimony atoms, as mentioned in Chapter 2.5, is approximately 4.60 Å in the $[\bar{1}10]$ direction. The distance between two planes in the [110] direction is half of that, i.e., 2.30 Å.

In Figure 5.3 (a), a close-up image with atomic resolution is provided. Individual Sb atoms are visible. Neither oxygen nor defects in the atomic lattice are observed, resulting in a perfect rectangular lattice of Sb atoms. The rectangular arrangement of the Sb atoms corresponds to the expected unit cell for the (110) plane. Based on a line profile along the white arrow in Figure 5.3 (a) (line profile shown in Figure 5.3 (c)), as well as a
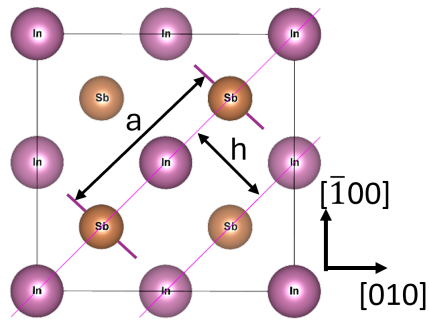
Figure 5.2: View of the InSb unit cell from the [001] direction. The (110) and the (220) planes are indicated with pink lines. a indicates the distance between two atoms of the same element in the $[\bar{1}10]$ direction. h indicates the distance between two atomic layers in the [110] direction.

FFT of the STM image (see Figure 5.3 (b) and the corresponding profile in Figure 5.3 (d)), the distance between Sb atom rows can be determined as 6.9 ± 0.1 Å. Additionally, the shorter distance between the Sb atoms can be determined as 4.7 ± 0.1 Å from the FFT transformation. Both values are slightly higher than the respective theoretical values of 6.48 Å and 4.60 Å, respectively. These deviations could be due to incorrect calibration of the STM. However, the values suggest that there is no reconstruction on the clean InSb(110) plane, as expected for this non-polar surface.
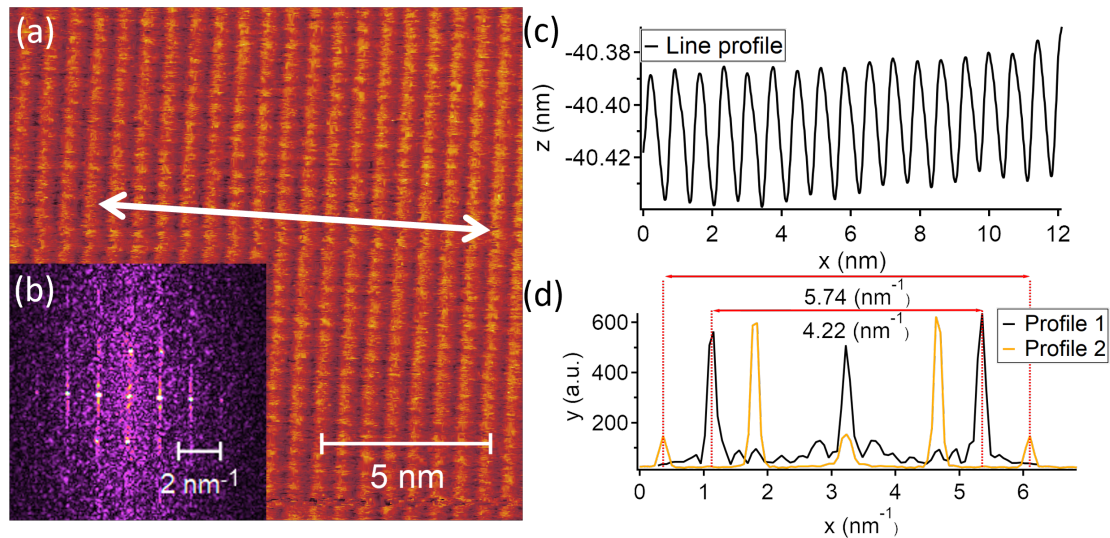
Figure 5.3: (a) STM image with atomic resolution from the clean InSb (110) surface. (b) FFT image generated from image (a). (c) Line profile taken along the white arrow in (a). (d) Line profile taken across two perpendicular lines through the centre of the FFT image. $V = -1.3$ V, $I = 150$ pA.

Interestingly, a higher step density was observed at the centre of the sample surface, as shown in Figure 5.4.

Instead of larger flat planes, a complex structure composed of many overlapping terraces is visible. Figure 5.5 (a) provides a close-up view along these terraces with an even further zoom-in with atomic resolution in one dimension (Figure 5.5 (b)), corresponding to the area marked by a white rectangle in Figure 5.5 (a). The white spots in the image are likely residues from the cleaved sample that are lying on the sample surface. These were observed exclusively on a single InSb(110) sample but consistently on that

Figure 5.4: STM image from the clean InSb taken in the centre of the sample surface. A high step density is observable. $V = -2.5$ V, $I = 130$ pA.

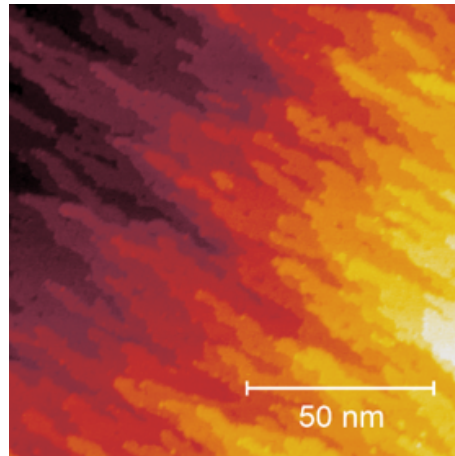sample. Notably, in the zoom-in shown in Figure 5.5 (b), the terraces can be seen to form approximately a 45-degree angle with the atomic chains. Height profiles taken along the arrows in Figure 5.5 (a) (see Figure 5.5 (d)) show a peak in brightness at the edge of the terraces.
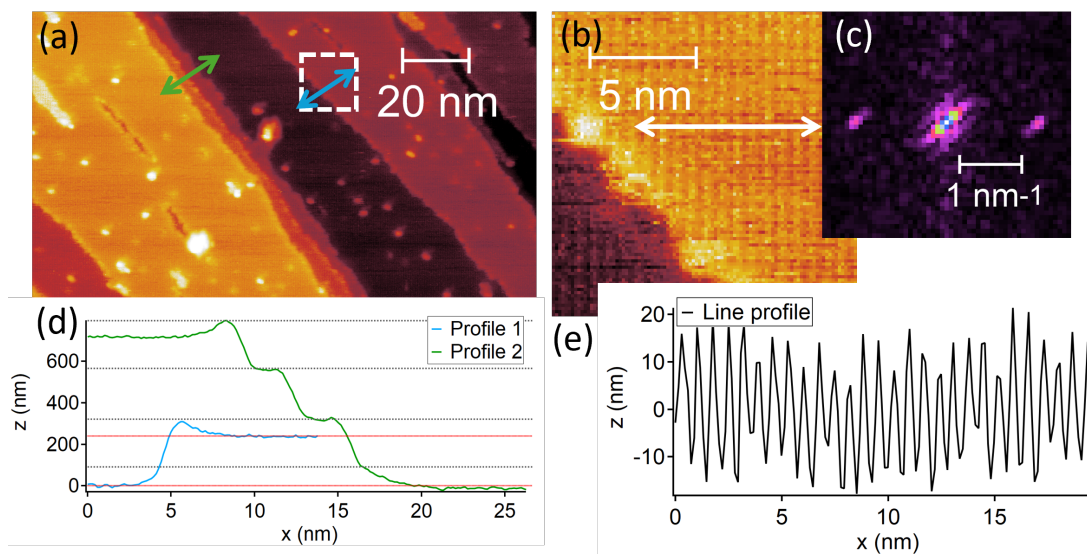
Figure 5.5: (a) STM images from the clean InSb (110) surface taken at the centre of the sample. (b) Zoom in into image (a) in the white square. (c) FFT image generated from image (b). (d) Height profile taken along the arrows in (a). (e) Line profile taken along the white arrow in (b). $V = -2.5$ V, $I = 100$ pA.

By comparing with the retrace images, i.e. the images taken when moving the STM tip backwards the same scanning lines, a cause by a feedback overshoot of the STM system could be excluded, since the same bright edges are observed there. Instead, a charging caused by dangling bonds at the edge of the terraces could cause the measured change in height at the terrace edge. In a distance, left and right from the terraces, the charging disappears and the height profile goes back to a steady value. Since this

relaxation is not possible between the short terrace steps in the height profile 2, one has to assume that the height profile is still disturbed by charging. Therefore, the height of the steps in profile 2 are determined between the increased value at the beginning of the step and before the relaxation of the system at the end of the step (see red lines in the height profiles). These measruements again result in an average step height of 230 ± 9 pm, matching the height of one monolayer in the (110) plane.

Table 5.1: Step heights extracted from the height profiles along the blue arrows in Figure 5.5 (a) (Profiles are shown in Figure 5.5 (d)). The heights from profile 2 are taken from the top to the bottom.

	Profile 1	Profile 2, 1	Profile 2, 2	Profile 2, 3
Step height	232 pm	232 pm	239 pm	223 pm

The observed atomic chains in Figure 5.5 (b) again show no defects or signs of oxides. A line profile along the white arrow (Figure 5.5 (e)) and an FFT transformation reveal an atomic row spacing of approximately 6.9 ± 0.1 Å. This again shows the same deviation from the theoretical value as in Figure 5.3, supporting the hypothesis that the STM is poorly calibrated.

On the surfaces with increased step density, the same parameters are measured as in the flat regions, which is expected since it is the same sample.

5.2 STM Analysis after Bi Deposition

As described in Section 4.2, Bi was evaporated onto the sample surface at a temperature of approximately $250°C$ for 10 minutes.

Figure 5.6 (a) shows an STM image of the InSb(110) surface after Bi deposition. Clear atomic rows are visible without significant defects. A continuous upper layer with isolated larger terraces, aligned with the atomic lattice, is observed. A height profile along the blue arrow in Figure 5.6 (a) (see Figure 5.6 (d)) shows a step height of 228 ± 5 pm. This corresponds to the height of a monolayer of the InSb(110) substrate, suggesting that these steps originate from the underlying substrate rather than a Bi layer.

An enlarged view of the area marked by a white rectangle in Figure 5.6 (a) is shown in Figure 5.6 (b). Based on this enlargement, an FFT transformation was performed, and a line profile along the white arrow was taken (see Figure 5.6 (c) and Figure 5.6 (e), respectively). These reveal an atomic row spacing of 13.7 ± 0.4 Å and 13.8 ± 0.3 Å. This corresponds to double the row spacing of pure InSb, suggesting a possible Xx2 reconstruction, where X could not be identified because the spacing along the $[1\bar{1}0]$ direction could not be determined.

This Xx2 reconstruction indicates that Bi is indeed present on the surface and that it is no longer pure InSb, which does not exhibit reconstruction on the (110) surface. The Bi structure appears to follow the underlying substrate structure, as evidenced by both the reconstruction and the step height. An Xx2 reconstruction for Bi is expected because Bi atoms are larger than In or Sb atoms, making it difficult for them to fit into the 1x1

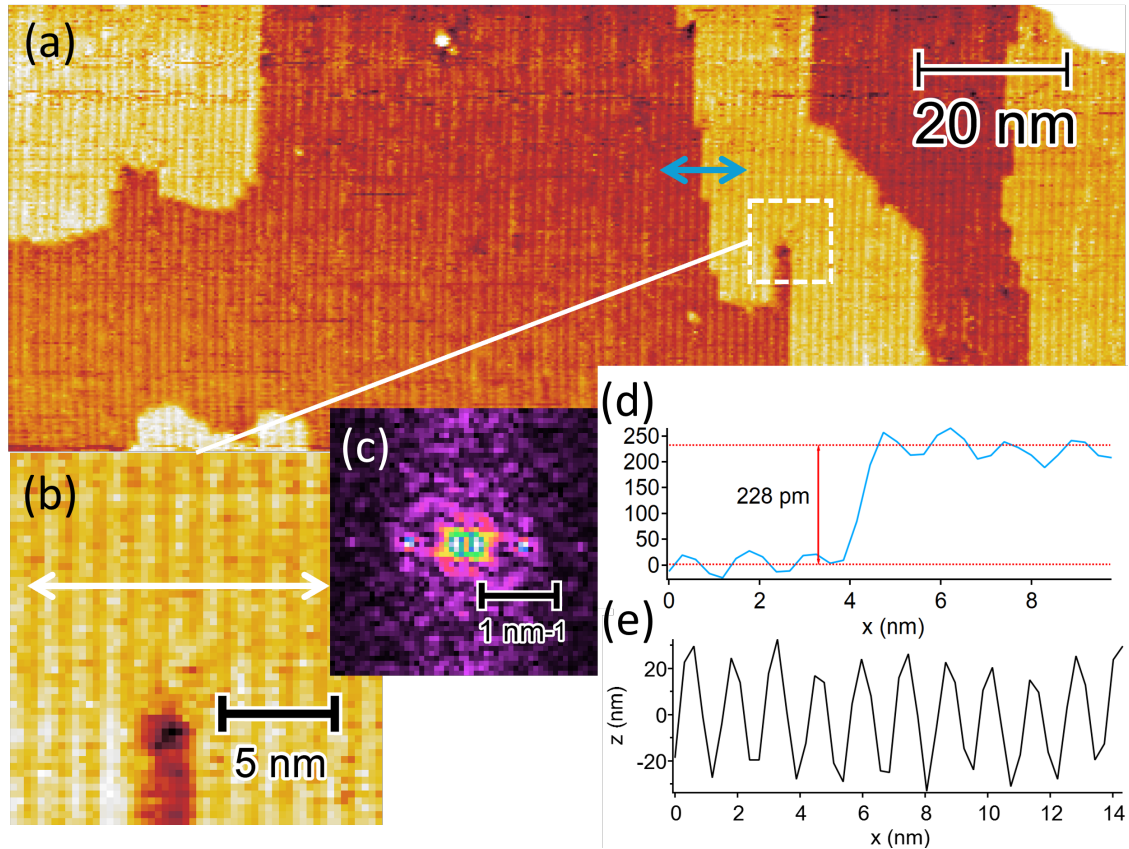Figure 5.6: (a) STM images taken at the edge of the sample from the InSb (110) surface after Bi deposition at about $250°C$ sample temperature. (b) Zoom in into image (a) in the white square. (c) FFT image generated from image (b). (d) Height profile taken along the blue arrow in (a). (e) Line profile taken along the white arrow in (b). $V = -1.8$ V, $I = 130$ pA.

InSb structure. The presence of Bi on the surface will be further verified through XPS analysis.

From previous works, like Betti et al.'s[50], the Xx2 reconstruction can be presumed to be a 1x2 reconstruction.

Instead of the previously described reconstruction, numerous islands were observed at the centre of the sample surface, as shown in Figure 5.7 (a). These islands are approximately rectangular, with average dimensions of 15 ± 5 nm by 40 ± 10 nm. At a closer look at the islands on the right side of Figure 5.7 (a), one can see that every two islands build a doublet with the same shape of the lower left corner of the island. This indicates, that these are not different islands but are caused by a double-tip effect. This double-tip effect was observed in all island-containing STM images of Bi-InSb.

Height profiles taken at these islands may therefore represent a convolution of the STM double-tip effect and the actual island height. The height profiles, such as those taken along the arrows in Figure 5.7 (a) (shown in Figure 5.7 (e)), reveal step and island heights ranging from 420 pm to 1.84 nm. These are higher than the height of a monolayer of InSb, as well as the distances between the (110) and (111) planes of an
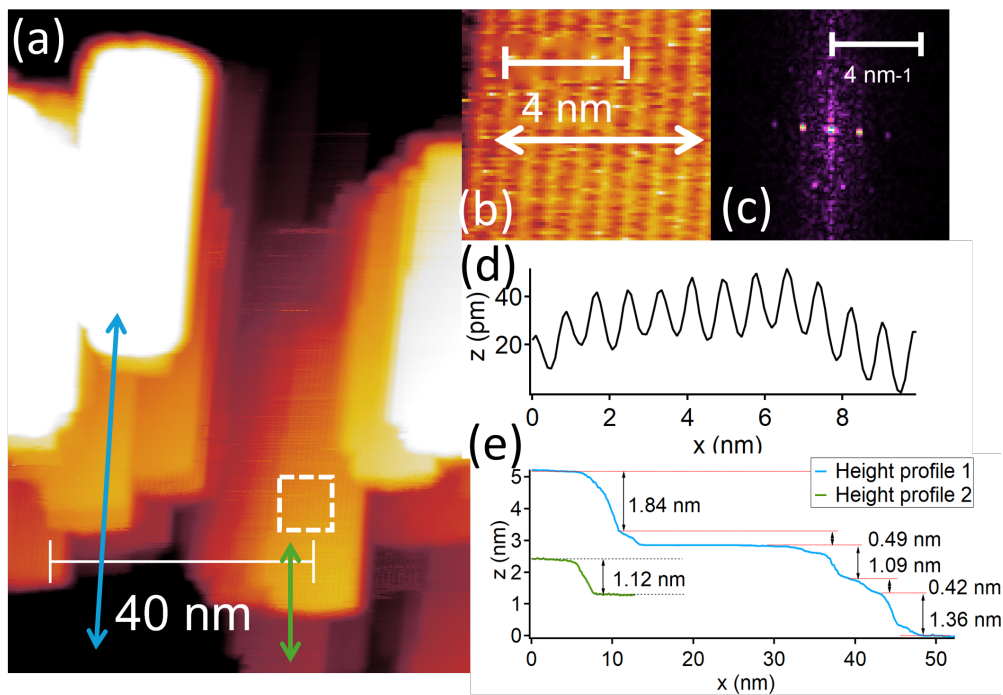
Figure 5.7: (a) STM images taken at the centre of the sample from the InSb (110) surface after Bi deposition at about $250°C$ sample temperature. The position on the sample is marked with a black cross at the sketch at the right. (b) Zoom in into image (a) in the white square. (c) FFT image generated from image (b). (d) line profile taken along the white arrow in (b). (e) Height profile taken aling the arrows in (a). $V = -1.7$ V, $I = 140$ pA.

ideal Bi crystal, which would be 335 pm and 394 pm, respectively.[51] Therefore, one can conclude that these structures are higher than one or two atomic layers.

The steps themselves are flat, as can be seen in the enlarged view of Figure 5.7 (a), which is shown in Figure 5.7 (b). There is one-dimensional atomic resolution, again showing a surface without defects and with a continuous rectangular arrangement of atoms. Comparing the orientation of the atomic rows and the islands reveals that the islands are aligned with the atomic rows and are not tilted by 45 degrees, as the InSb terraces are.

FFT analyses and a line profile from Figure 5.7 (b) result in an atomic row spacing of 8.1 ± 0.1 Å. This differs from the atomic spacing of 6.9 ± 0.1 Å of the underlying InSb substrate, as well as from the Bi–Bi bond length measured for elemental Bi, which is approximately 3 Å.[52;53]

Since these islands differ in shape from the underlying InSb terraces and the determined atomic row spacing also differs from that of the substrate and is not a reconstruction of it, these Bi structures appear to be independent of the underlying substrate. This could be supported by XPS data, which should predominantly show Bi-Bi bonds.

The difference between the Bi structures observed at the surface edge and in the centre could be caused by the difference in terrace density. However, since the underlying InSb structures were atomically identical, it is more likely that a thermal gradient exists

between the edge of the sample and the interior, leading to different bonding types and thus different structures. As Benter et al.[23] found through XPS analysis results, the bonding types of Bi on III-V surfaces vary with the sample temperature during deposition.

Another region was observed on the Bi-InSb surface, featuring both a wide area as shown in Figure 5.6 and islands as shown in Figure 5.7 (see Figure 5.8)
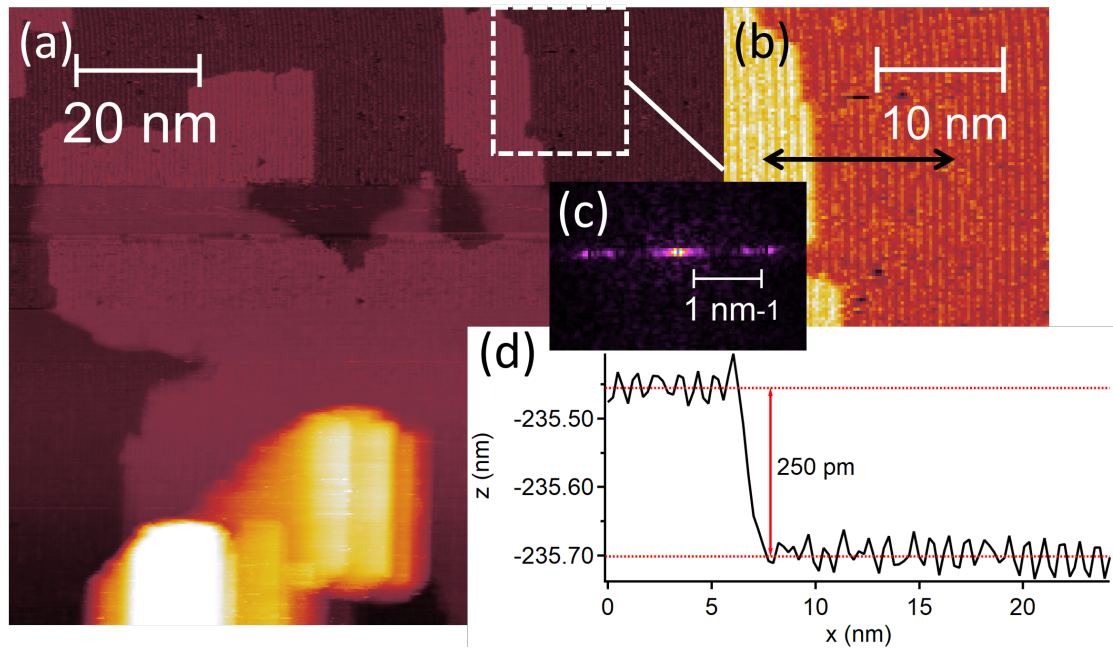
Figure 5.8: (a) STM images taken after Bi deposition at about $250°C$ sample temperature. Both flat areas as well as elongated islands are visible. (b) Zoom in into image (a) in the white square. (c) FFT image generated from image (b). (d) line profile taken along the arrow in (b). $V = -2.0$ V, $I = 1000$ pA.

In the flat region, atomic resolution was achieved, allowing the determination of the atomic row spacing and step height through magnification (Figure 5.8 (b)), along with line profile and FFT analysis. A step height of 230 ± 5 pm was again determined, which corresponds to that of the underlying substrate. In contrast to the purely flat regions depicted in Figure 5.6, the line spacing was determined to be approximately 8.3 ± 0.1 Å, which is more consistent with that of the Bi islands. One can assume that more Bi-Bi bondings are formed than Bi bondings to the substrate atoms In and Sb, which could again be caused by a heat gradient.

5.3 XPS Analysis of the FlexPES Sample

After examining the surface structure of a sample heated during bismuth evaporation in the previous section, we will now investigate the chemical composition of a similar sample to gain insight into the bonding partners. This will be achieved through the analysis of XPS data obtained at the FlexPES beamline at MAX IV. In XPS data, the position of peaks shows which elements are present. Within a core level peak for an element, the type of bonds and the bonding partners of the atoms can be determined by the chemical shift. A core level peak is made up of different peaks, which originate from atoms of the same element, but which have different bonding partners, causing this chemical shift in the spectrum. The separation of these individual peaks in the core level spectrum and the determination of the origin of these peaks therefore helps to identify the bonding types within the sample. The area of the individual peaks changes with the number of atoms with this type of bond. By normalising to the total core level peak area, it is therefore possible to determine how the ratio between different bonds of an element within the sample changes with different processing steps.

As described in Chapter 4, for the FlexPES sample, the bismuth deposition was conducted in several steps, as the bismuth content after the initial deposition was barely detectable.

5.3.1 The Core Levels of the FlexPES Sample

XPS data for the core levels In 4d, Sb 4d, and Bi 5d were acquired at photon energies of 340 eV and 130 eV, with the measurements at 130 eV exhibiting higher surface sensitivity, as explained in Section 2.2. Therefore, these measurements will be examined in greater detail in the following analysis. According to the determination by the FlexPES beamline team, the instrumental broadening of the binding energies for the measurements done at 130 eV is approximately 21 meV.

The calibration of the data was performed using gold reference measurements from a gold sample, located on the sample holder, taken at a photon energy of 340 eV. The In 4d bulk peaks were identified in the spectra fits for 130 eV and 340 eV, and the 130 eV In 4d bulk peaks were aligned to the same energy as the gold-calibrated 340 eV data.

The spectra, taken at binding energies between about 15 eV to 35 eV were normalized to the In 4d peak. Multiple measurements were conducted for each step and averaged. It became evident that the Sb 4d peaks varied for the same preparation step across different measurements, with new peaks appearing in some measurements. As these shoulders appeared intermittently and were not reproducible, they are likely artefacts, possibly due to charging effects on the sample. Consequently, the Sb 4d peaks for this sample are unsuitable for analysis and will not be included in subsequent investigations.

Figure 5.9 shows spectra around the In 4d and Bi 5d peaks, normalized to the higher In 4d peak. For the clean sample as well as after Bi deposition, an In doublet is visible around 18 eV. An additional Bi doublet at approximately 26 eV appears after Bi deposition. Especially the In peaks for the clean sample and the Bi doublets after the

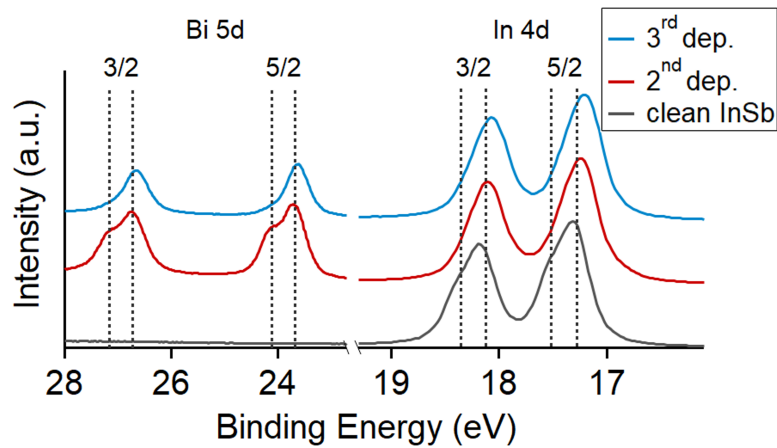second deposition show an asymmetry with extra shoulders, indicating the presence of different components.

Figure 5.9: Bi 5d and In 4d core level spectra for the clean InSb sample as well as after different deposition steps, taken with a photon energy of 130 eV. The spectra are normalised to the In 4d peak and the position of the different peaks, extracted from fits, are marked by dashed lines. The reduction of a shoulder at higher binding energies after the second deposition and after the third deposition for the In 4d and Bi 5d peaks, respectively, is visible. A shift of the In peaks after deposition is visible.

A reduction in a shoulder at higher energies is observed for the In 4d peak after bismuth deposition, suggesting that there are surface peaks present at higher binding energies. With bismuth present, fewer In atoms are on the sample surface, contributing less to the surface peak. This assumption is corroborated by a reduced prominence of this shoulder at higher photon energy of 340 eV compared to 130 eV, shown in Figure 5.10.
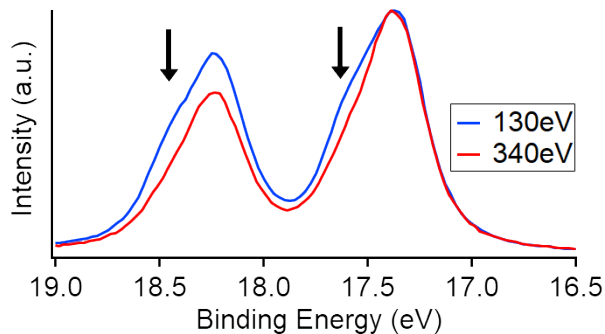
Figure 5.10: In 4d core level spectra taken at 130 eV and 340 eV. A reduction of the peaks at higher binding energies, indicated with black arrows, is visible from 130 eV to 340 eV.

Regarding the Bi 5d core level, it is notable that the observed Bi peak intensity is decreased after the third deposition compared to the second deposition. This indicates a reduced amount of bismuth on the sample, contrary to the expectation following bismuth deposition. It is hypothesized that the prolonged heating of the sample before the third deposition led to the release of bismuth from the sample. This type of bismuth release upon heating has been previously observed by Benter et al.[23].

5.3.2 Fitting for the Core Levels

The In 4d and Bi 5d core levels were fitted for the individual processing steps using a Voigt function as explained in Section 3.3. The branching ratio, spin-orbit splitting, and Lorentzian FWHM were kept constant for each core level. The parameters used for the fits are provided in the Appendix A.1. The fits for the In 4d core level are shown in Figure 5.11 (b). For the pure InSb sample, two peaks are necessary, with the higher binding energy (BE) peak identified as the surface peak, indicating that the second peak must be the In-Sb bulk peak.
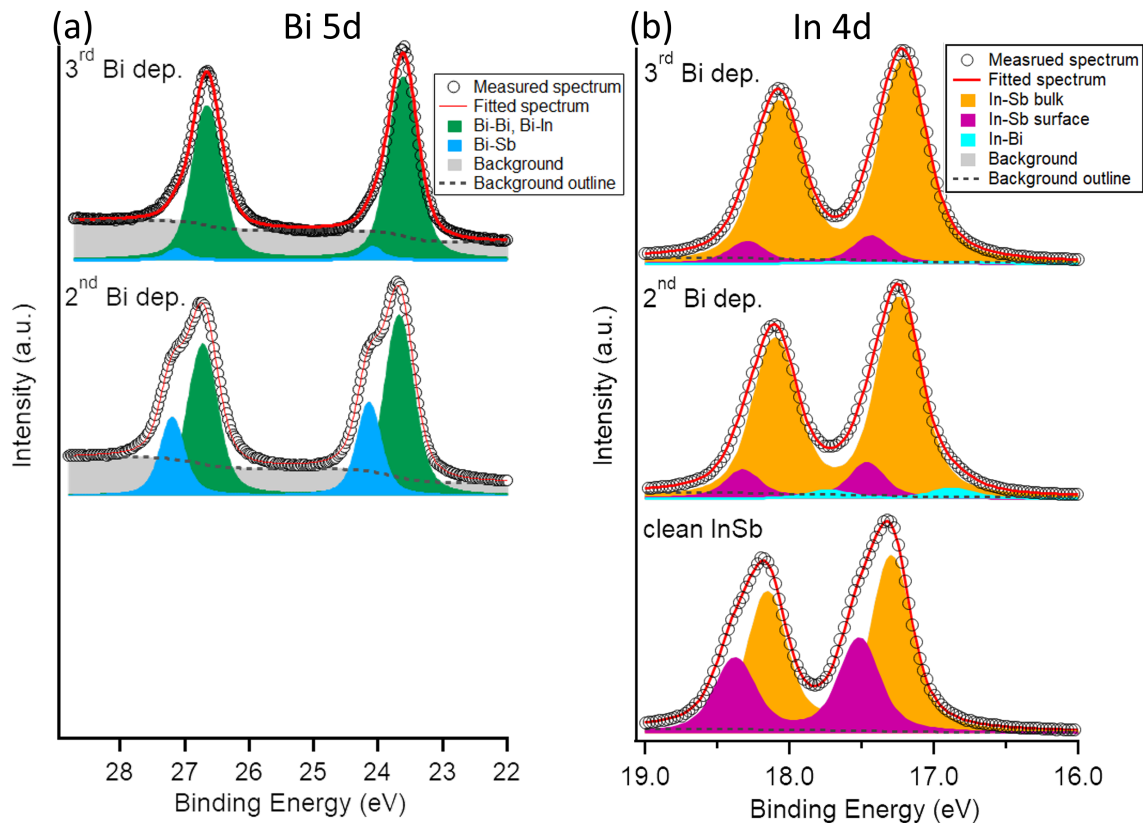
Figure 5.11: Fit of (a) Bi 5d and (b) In 4d core level spectra after different processing steps as labelled. The spectra are normalised. A third peak appears at lower BE for the In 4d core level after Bi deposition. The peak at higher BE for Bi 5d decreases after the third deposition.

Upon the second Bi deposition, the surface peak significantly reduces, while a third peak appears at lower BE. This third peak almost entirely disappears upon the third deposition. This third peak can be attributed to an In-Bi bond, confirmed by literature values.[54] The reduction of this peak after the third deposition aligns with the observed decrease in the Bi 5d peak. Considering the relative areas under the three In 4d peaks (see Table 5.2), it is notable that the surface peak decreases along with the In-Bi peak relative to the bulk peak. A possible explanation is that the remaining bismuth transitions from bonding with In to bonding with Sb or other bismuth atoms. In the upcoming analysis of the Bi 5d core levels, a decrease in the Bi-Sb peak relatively to the Bi-Bi can be observed, a transition to Bi-Bi bondings is more likely.

Table 5.2: Relative peak area of the peaks in the In 4d spectrum.

	clean InSb	2nd Bi dep.	3rd Bi dep.
In-Sb bulk	0.648	0.837	0.889
In-Sb surface	0.352	0.122	0.098
In-Bi		0.041	0.013

For further analysis, the fits of the Bi 5d core levels are considered (see Figure 5.11 (a)). Here, two peaks per branch are observed, with the peak at higher BE significantly losing intensity after the third deposition. The relative area under the peaks shows the higher BE peak's proportion decreases from 30% to under 5% after the third deposition. Given the decrease in the In-Bi peak in the In 4d core level towards the third deposition, one could speculate that the higher BE Bi peak corresponds to the Bi-In bond, while the lower BE peak corresponds to the Bi-Bi bond. However, this contradicts the peak arrangement observed by Richter et al.[54]. Without data for the Sb 4d peaks, the influence of Sb cannot be analysed, which is necessary for a clear identification of the peaks. The final analysis and identification of the peaks is therefore postponed to the analysis of the Bloch data in the next Section.

5.3.3 Structural Analysis with LEED Data

LEED patterns were also recorded for the various processing steps, shown in Figure 5.12. After the second deposition, a weak 1x3 reconstruction is visible, which disappears after the third deposition. This could be due to the previously noted reduction of bismuth on the sample surface, or due to a disordered structure of Bi-Bi bonds. Such a Bi-Bi structure could not be very thick, as the InSb structure remains clearly visible in LEED.
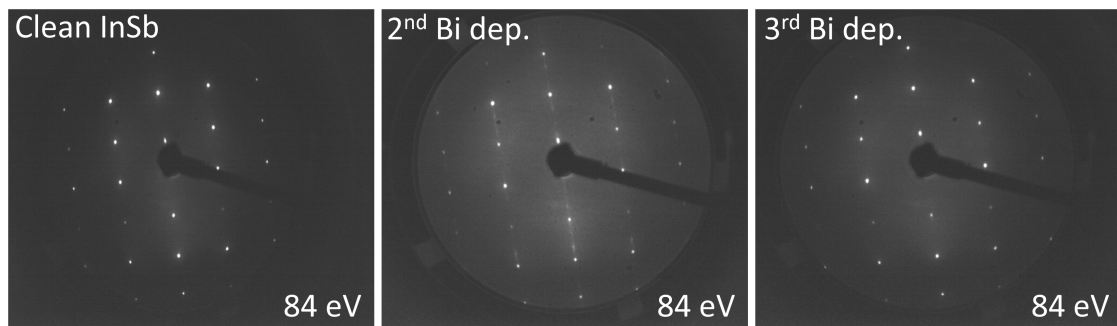
Figure 5.12: LEED images taken of the clean InSb, after the second and third bismuth deposition, respectively. The beam energy is given in the lower right corner of each image. After the second Bi deposition, a 1x2 reconstruction is visible by additional weaker spots between the spots of the substrate.

Unlike the sample discussed in the STM measurements in Chapter 5.1, this sample shows a 1x3 reconstruction despite similar processing steps being used. It is suspected that due to the inaccurate temperature determination in the FlexPES measurements,

the actual temperatures were significantly lower than originally assumed. However, this contradicts the findings of Betti et al.[50], who observed a transition from 1x2 to 1x3 reconstructions at higher annealing temperatures. This discrepancy can be caused by the different heating duration. While the sample of this experiment was heated for more than 20 min prior to every deposition step, Betti et al. heated their sample for much shorter times of about 5 min.[50]

5.4 Analysis of the Bloch Sample

At the Bloch beamline at MAX IV, a different sample was investigated, which was kept at room temperature during the Bi evaporation and subsequently annealed multiple times (see Chapter 4 for details). These measurements were conducted at a different beamline than the previous ones because further characterisations were performed on this sample, which are beyond the scope of this work.

In this series of measurements, no reference measurements on gold could be taken, so the peak positions were determined based on the FlexPES In 4d peaks of pure InSb. The energy broadening for the Bloch data set is comparable to the energy broadening of the FlexPES data, that is approximately 21 eV.

5.4.1 The Core Levels of the Bloch Sample

Figure 5.13 shows the normalised Sb 4d, Bi 5d, and In 4d core levels at a photon energy of 130 eV after the different processing steps, i.e the clean substrate and after the subsequent annealing steps upon Bi deposition. The main changes are visible between the clean sample (in black) and after Bi deposition. A shoulder at lower binding energies (BE) is visible for Sb 4d (and at higher BE for In 4d), which disappears after Bi evaporation. For a more detailed analysis, the Sb 4d, In 4d, and Bi 5d core level peaks were fitted for a photon energy of 130 eV.
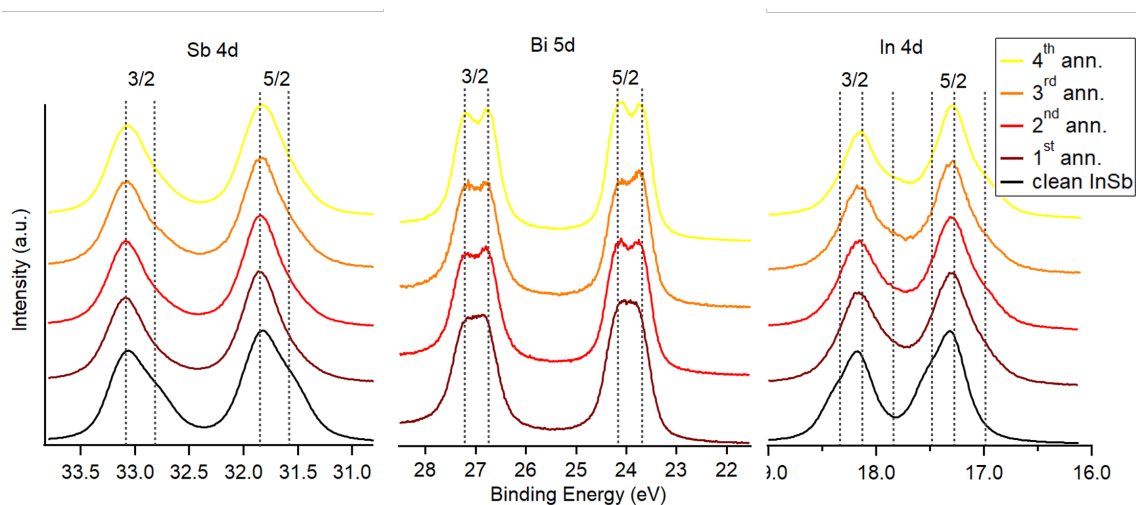

Figure 5.13: Normalised spectra of Sb 4d, Bi 5d and In4d core levels after different processing steps, all normalised to their highest peak respectively. The sample was at room temperature during the bismuth deposition and was annealed in separate steps. Peaks positions, which were determined during fitting, are marked with dashed vertical lines.

5.4.2 Fitting of the Core Levels

The fits for the Sb 4d, In 4d and Bi 5d core levels for the clean InSb sample, as well as after Bi deposition and subsequent annealing steps, are shown in Figure 5.14.

In the Sb 4d core level two peaks were identified, consistently appearing at the same binding energies of 31.57 eV and 31.85 eV for all processing steps. The parameters used for the fits are provided in Chapter A.1 of the Appendix. Both in the fits and the relative peak areas (see Chapter A.2 of the Appendix), it can be seen that the peak at lower BE is significantly reduced after Bi deposition compared to pure InSb, but it regains intensity during the annealing steps.
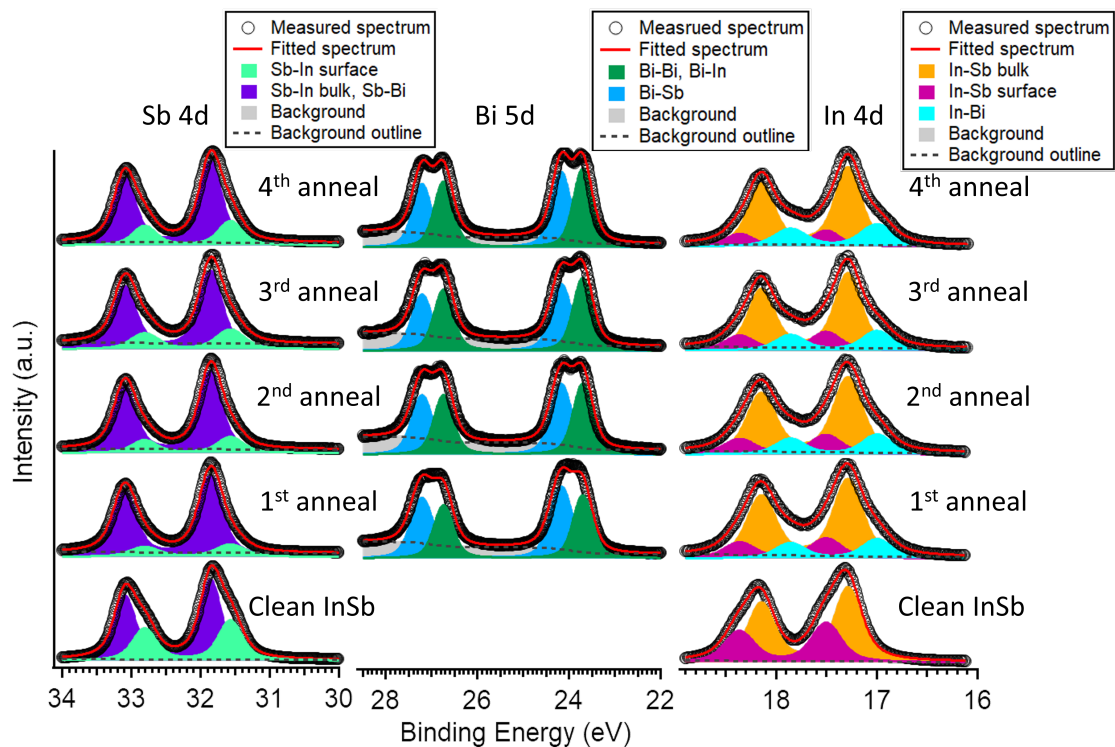
Figure 5.14: Normalised Sb 4d, In 4d and Bi 5d core level spectra, showing raw data and fitted components, taken at a photon energy of 130 eV for different processing steps. The peaks were identified as clarified by the legends. The Bi deposition occurred before the 1st anneal.

The In 4d fits show two peaks for pure InSb and an additional peak after Bi deposition, which aligns with observations from the FlexPES sample. The positions of all three peaks remain constant throughout the processing steps, similar to the Sb 4d peaks. However, the positions of the outer peaks relative to the middle peak differ by approximately 0.05 eV (higher BE) and 0.13 eV (lower BE) from the FlexPES data. This discrepancy can partly be attributed to measurement inaccuracies but may also result from differing chemical environments between the two samples. A plausible explanation for this shift is currently not available to the author. The peak intensities and relative peak areas indicate an increase in the peak at lower BE and a relative decrease in the other two

peaks during annealing.

In the Bi 5d fits, as in the FlexPES data, two peaks are identified, showing similar intensity. Over the course of the annealing steps, the peak at lower BE gains prominence.

As previously determined in the FlexPES data, for the In 4d core level, the peak at higher BE can be identified as the surface peak, the middle peak as the In-Sb bulk peak, and the peak at lower BE as the In-Bi peak, as previously established by Richter et al. and others.[54;55] Comparing with literature values, it can be inferred that the Bi-Sb peak lies at higher BE than the Bi-Bi or Bi-In peak.[56;23;22]

FlexPES

	Bi-Bi, Bi-In	Bi-Sb	In-Bi
Clean	0	0	0
2nd dep.	0.694	0.305	0.041
3rd dep.	0.954	0.046	0.013

BLOCH

	Bi-Bi, Bi-In	Bi-Sb	In-Bi
Clean	0	0	0
1st ann.	0.437	0.563	0.161
2nd ann.	0.483	0.517	0.166
3rd ann.	0.509	0.491	0.163
4th ann.	0.510	0.490	0.198

Table 5.3: relative peak area for selected peaks from the fitted FlexPES and BLOCH data. The colour of the cells indicate the size of the value in respect to the peak areas for the same peak during another processing step. It is visible that the peak areas for the Bi 5d core level behave similarly for FlexPES and BLOCH, while the In-Bi peaks show contrary behaviour.

Comparing the changes in the In-Bi peak in the In 4d spectrum of the FlexPES and Bloch data with the changes in the area of the Bi 5d peaks in both measurements (see Table 5.3), it is observed that for both samples (FlexPES and Bloch), the Bi 5d peak at lower energies increases relative to the other peak, upon subsequent deposition at elevated temperatures or consecutive annealing. Simultaneously, the behaviour of the In-Bi peak in the In 4d spectrum differs for both samples: while the peak decreases in the FlexPES measurements, it increases in Bloch. This seemingly contradictory behaviour of the In-Bi and Bi peaks between the two samples suggests that the Bi-In peak in the Bi 5d spectrum overlaps with another peak, which behaves differently for Bloch and FlexPES. Considering the relative positions of the Bi-Sb and Bi-Bi peaks in literature, as mentioned above, it is plausible that the Bi-In peak overlaps with the Bi-Bi peak and corresponds to the peak at lower BE, while the second peak at higher BE represents Bi-Sb bonds.

Based on literature values and the significant decrease in the peak at lower BE, the Sb 4d peaks at higher BE and lower BE can be assigned to the Sb-In bulk and the Sb surface peak, respectively.[22] From the Bi 5d spectra, it is evident that a non-negligible amount of Sb-Bi bonds exists, which should also be visible in the Sb 4d spectrum. As the Bi-Sb peak in the Bi 5d spectrum decreases with annealing, the Sb-Bi peak in the Sb 4d spectrum must also decrease. However, since the peak previously identified as the surface peak at lower BE increases with annealing, and the sum of the Bi 5d peaks does not significantly decrease compared to the Sb peaks, it can be assumed that the Sb-Bi

peak overlaps with the Sb-In bulk peak.

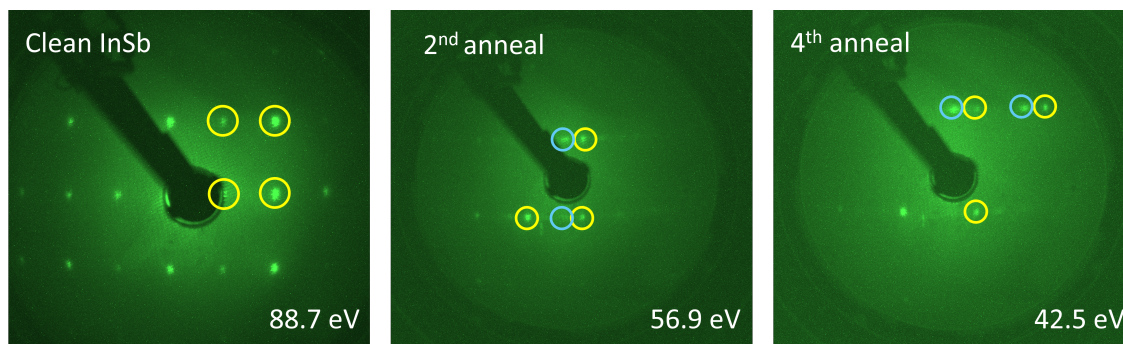## 5.4.3 Structural Analysis with LEED Data

Figure 5.15: Selected LEED images taken on the clean InSb surfaces and in-situ during the annealing steps indicated at the top of the pictures. With yellow circles, points of the InSb substrate are marked. New occurring spots, during the annealing are marked with blue circles. From their position, a 1x3 reconstruction can be identified.

For the Bloch data, in-situ LEED recordings were also taken during each annealing step. After Bi deposition, additional LEED spots are observed, as marked with blue circles in Figure 5.15. Since the aspect ratio of the substrate structure's spots must be maintained, it can be concluded that an additional peak has formed closer to one side of the substrate spots. Based on the position of the spots, a 1x3 reconstruction can be inferred, although every second spot of the reconstruction is missing. This LEED pattern remains unchanged throughout the annealing steps.

5.4.4 Bloch STM Measurements

The Bloch measurement setup also enables STM measurements of the same sample used for XPS measurements without removing it from the UHV. An STM image of the sample after all processing steps is shown in Figure 5.16. However, the STM only produced distorted images, where the image appeared to bulge and one side seemed compressed compared to the other. Therefore, only a small portion of the image was usable and quantitative evaluations of the measurements were difficult. The image shows broader terraces orientated along the atomic chains. An magnification on one of the terraces is given in Figure 5.16 (b), revealing pairs of atomic rows with a missing row between each pair.

Since the distortions of the image are hardly visible in the enlarged section shown in Figure 5.16 (b), a line profile and FFT analysis were performed. The line profile indicates an average atomic row spacing of approximately 13 ± 5 Å, corresponding to a 1x2 reconstruction. The FFT analysis determined three different values, 13 ± 1 Å, 19.6 ± 0.5 Å and 39.5 ± 0.5 Å. The 13 ± 1 Å correspond to the average atomic row spacing determined with the line profile in Figure 5.16 (c). The missing rows cause a periodic pattern, which repeats itself every third row, leading to a period length of
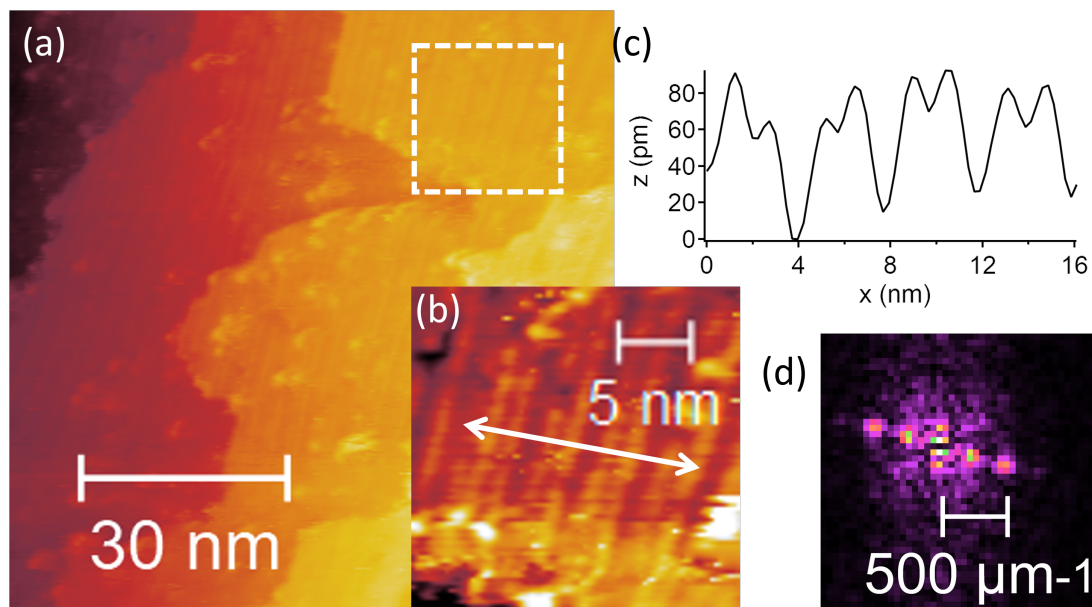
Figure 5.16: (a) STM Image of the BLOCH sample after all annealing processes. The STM images is distorted, due to some errors in the STM setup. (b) Zoom into (a) as marked with a white square. A line profile shown in (c) was taken along the white arrow in (b). (d) FFT image generated from image (b). $V = -1.6$ V, $I = 160$ pA.

$3x13$ Å $= 39$ Å, which corresponds to the 39.5 ± 0.5 Å determined with the FFT analysis. Taking into account that the distance of the atomic rows was measured to 13 ± 5 Å, i.e. 2x the spacing of the atomic rows of the substrate, an Xx6 reconstruction can be assumed from this periodic pattern every three atomic rows. The 19.6 ± 0.5 Å determined in the FFT analysis is not visible in the image itself (Figure 5.16 (b)) and is roughly the half of the determined 39.5 ± 0.5 Å. Therefore, it is concluded that this value is an overtone and thus an artefact of the FFT and can be disregarded.

The measured line spacings suggest an Nx6 reconstruction, whereas a 1x3 reconstruction was deduced from the LEED pattern. A 2x6 reconstruction exhibits the same aspect ratios as a 1x3 reconstruction in a LEED pattern but features more closely spaced spots at the same kinetic energy. By taking into account the magnification of the LEED pattern due to the altered kinetic energy in Figure 5.15, a 1x3 reconstruction can be endorsed. Consequently, the miss-calibration of the STM leads to an approximate doubling of the measured distances. Thus, the measured 13 ± 1 Å and 39.5 ± 0.5 Å correspond, upon correct calibration, to 6.48Å and approximately 19.5Å, respectively.

5.4.5 Reconstruction of the Bloch Sample Surface

Based on the XPS data, it is known that bismuth atoms are present on the surface of the sample, and the observed structures are therefore clearly bismuth-related. The bismuth atoms primarily bond with the antimony atoms, evident by the XPS data, meaning that the bismuth binds directly to the substrate rather than forming a metallic bismuth film. Since the bismuth follows the underlying substrate structure, it can be assumed that in a given atomic row, each bismuth atom bonds with an underlying antimony atom.

However, the precise positioning of the bismuth atoms relative to the antimony atoms cannot be determined from the STM images and would require supplementary density functional theory (DFT) calculations.

The bismuth atoms are larger than the antimony atoms, which may lead to strain if the bismuth atoms follow the antimony structure. The absence of every third bismuth row could serve to relax this strain. It would allow the other two bismuth rows to have a greater distance between each other by slightly shifting into the gap to the right or left. A model for this structure is presented in Figure 5.17.
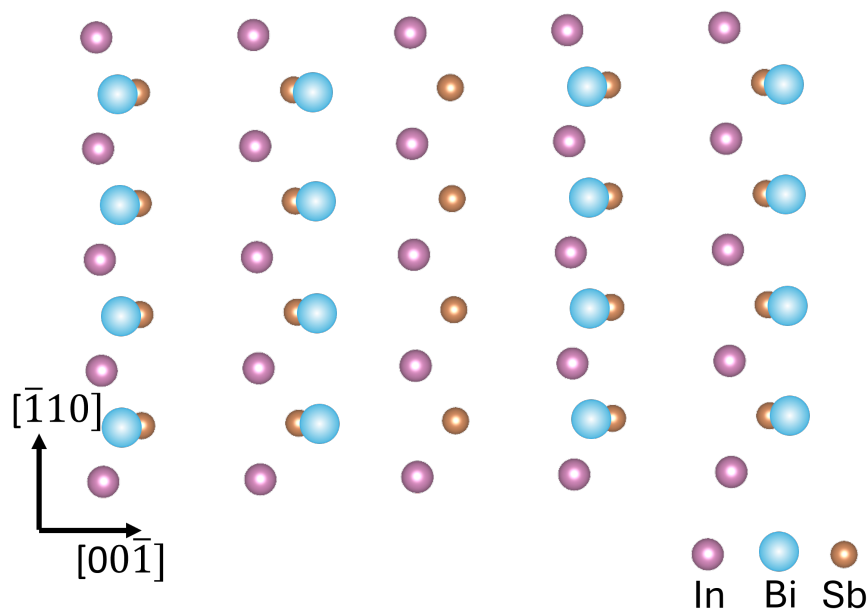
Figure 5.17: Top-view modell of the (110) plane of InSb with Bi. The correct position of the Bi atoms in respect to the Sb and In atoms is unknown.

This deviation of atomic row distances from the underlying substrate could be verified through calibrated STM images, which are, however, not available. A second LEED pattern, superimposed on the substrate pattern with a smaller spacing between the spots, could support this theory. The fact that this is not observed may be due to the poor quality of the LEED images, but also due to low bismuth coverage. Thus, LEED does not provide a definitive conclusion regarding the position of the bismuth atoms.

It is nonetheless interesting to note that, in contrast to the sample discussed in Chapter 5.2, where a 1x2 reconstruction was observed, an alternative mechanism has been identified here to accommodate the difference in size and bonding characteristics between the bismuth and antimony atoms.

6 Discussion

While the STM sample and the FlexPES sample were intended to be used as complementary techniques under similar conditions, differences in the formed reconstruction have already been revealed through the LEED images. While a 1x2 reconstruction was determined in the STM data, a 1x3 reconstruction is evident in the FlexPES data. These differing results are attributed to the lack of precise temperature control during the FlexPES measurements, where only a rough estimation of the temperature was possible. Due to the thickness of the sample holder and the protrusion of the examined sample surface, it is assumed that the temperatures in FlexPES were lower than those for the STM samples.

Interestingly, however, a significant reduction in the amount of bismuth was observed during the third deposition at low temperatures in the FlexPES sample. Desorption of Bi has so far only been significantly noted at temperatures above 250°C, to the best of the author's knowledge. [50;23] In the FlexPES data, a reduction in the number of Bi-Sb bonds was also observed, while the number of Bi-In and Bi-Bi bonds experienced comparatively little reduction. Therefore, it is assumed that prolonged heating of the sample before and during deposition favours In-Bi and Bi-Bi bonds over Bi-Sb. This is also confirmed by Bloch data, where a significantly higher proportion of Sb-Bi bonds was detected during deposition at room temperature, which decreased during heat treatments of the sample. It is noteworthy in Bloch that Bi-In bonds increase during heating, and, in contrast to the FlexPES sample, hardly any reduction in the Bi content was observed.

The observation of a 1x3 reconstruction after deposition at room temperature and subsequent heating to over $220°C$ was already noted by Betti et al., who also investigated Bi on InSb(110) surfaces. [50] They also observed a 1x2 reconstruction when heating at lower temperatures. Since no lower temperatures were used here, this observation could not be confirmed or refuted. At temperatures above $250°C$, Betti et al. observed the desorption of Bi and the recovery of the 1x1 structure of the substrate. In the FlexPES data, the 1x1 reconstruction was also observed again after the third deposition at $250°C$. Interestingly, however, the actual temperatures on the sample surface are assumed to be lower. If one assumes that the sample observed in FlexPES should correspond to the behaviour of Betti et al.'s samples, an approximate range for the sample surface temperature can be set. Betti et al. also observed a 1x3 reconstruction at $220°C$, which would limit the temperature to between $220°C$ and $250°C$. However, it should be noted that the heating durations in Betti et al.'s experiments were significantly shorter, at approximately 5 minutes per temperature value. [50]

Benter et al. also investigated Bi structures on InAs (110) for deposition at elevated sample temperatures and room temperature with subsequent heating. [23] Their observations largely align with those made in this study. They also observed that bonds

between Bi and the group V element tend to form more readily during deposition at room temperature, and heating the sample leads to a greater proportion of In-Bi bonds. They further observed that even at temperatures around $400°C$, Bi remained on the sample, which also corresponds with our observations from the Bloch data.

7 Summary

In this study, various methods of Bi deposition on InSb(110) surfaces were investigated using XPS, LEED, and STM measurements. STM measurements on the pristine InSb(110) surface revealed different structures between the edge and the centre of the sample. While the surface at the edge of the sample exhibited long, flat terraces, the centre consisted of many smaller terraces that appeared flaky. A difference in the surface morphology between different regions of the sample surface was also observed after deposition. At the edge of the sample, a 1x2 reconstruction was found, which still followed the underlying InSb terraces. Numerous bismuth islands were found more towards the centre of the sample, which differed in growth direction from the underlying terraces. The atomic row spacing of approximately $8\,\text{Å}$ deviates from that of InSb, suggesting that these structures form largely independently of the underlying substrate. An intermediate region was observed between these areas, where the top atomic layer still followed the InSb terraces but already exhibited the $8\,\text{Å}$ atomic row spacing of the Bi islands. The difference in these regions was contributed ot a potential temperature gradient on the sample surface.

XPS measurements at the FlexPES beamline of MAX IV were executed to investigate the chemical composition and bondings on the sample surfaces after Bi deposition at elevated sample temperatures. The core level peaks of the Bi 5d and In 4d could be identified, while the Sb 4d measurements had to be abandoned, due to measurement artefacts. A small amount of Bi-In bonds as well as Bi-Sb bonds were observed. The amount of Bi on the surface and the share of the Bi-In and Bi-Sb bonds on the Bi bonds decreased after a third deposition, most likely due to a longer heating of the sample at higher temperatures. For a deposition at room temperature, a higher amount of Bi-Sb bonds was discovered, with a change towards more Bi-In bonds after subsequent annealing. Additional STM imaging of this sample revealed a 1x3 reconstruction with every third row missing, likely to relieve strain from the incorporation of Bi atoms.

One aspect that remains unresolved after this study is the effect of heat on the desorption of bismuth from the InSb(110) surface. While the FlexPES sample showed a significant reduction of bismuth after prolonged heating before the third deposition, the bismuth content on the Bloch sample appeared unchanged despite heating to much higher temperatures of up to $400°C$ for several hours.

The XPS data revealed that the proportion of In-Bi bonds is increased when subsequently annealing the sample after deposition at room temperature.

Overall, a method was found that produces an increased proportion of In-Bi bonds, which are expected to contribute significantly to a substantial inverse band gap. Angle-resolved photoemission spectroscopy (ARPES) measurements where already conducted for the Bloch sample. Hereby, ARPES is a measurement technique where the emitted photoelectrons are detected angle-resolved, which conserves the information about their momentum parallel to the sample surface. The measurement of these electrons then gives

an image of the valence band structure on the sample surface, which contains information about aspects like band-splitting and the band gap size. The ARPES measurements of the Bloch sample have already shown a promising Rashba splitting, i.e. a splitting of the valence bands according to the electron spin. However, the analysis of these measurements is beyond the scope of this work.

8 Outlook

Although this work has advanced the understanding of bismuth structures on InSb(110), several aspects remain to be explored in future studies.

Due to the inability to determine the exact sample temperature for the FlexPES sample, the desposition parameters differed from those of the STM sample, resulting in a different surface structure, as evidenced by a 1x3 reconstruction observed in LEED: Reproducing the FlexPES sample measurement data in STM could provide insight into the precise surface structure of the sample. With the help of a newly integrated LEED in the STM setup, the temperatures of the FlexPES sample surface could be determined within a certain margin of error by generating a LEED pattern similar to that of the FlexPES sample. Since the STM measurements of the Bloch sample were distorted, reproducing these data in STM would also be beneficial, again using LEED as a reference.

Voltage-dependent STM measurements could provide better insight into the positions of In, Sb, and Bi atoms on the surface. In this study, STM measurements could not capture images at positive tunnelling voltage due to tip instabilities, which would otherwise make the position of the In atoms visible. Scanning tunnelling spectroscopy would additionally allow the measurement of the local density of states (LDOS) of the surface and thus the bandgap. This could help identify surface states and provide information on whether the bismuth structures are metallic or more semiconductor-like.[57]

ARPES enables the measurement of the surface band structure and the identification of Rashba splitting, which is particularly relevant for spintronic applications.[58] Measurements of the longitudinal conductance could also be relevant, as they can help identify a topological insulator.[59]

If the formation of a topological insulator is confirmed, the observed Bi structures could contribute to optimising energy use in electronic devices, due to the nearly lossless charge transport in topological insulators. A spin splitting, which could be verified through ARPES measurements, further opens the field of spintronics as a potential application area for the discovered structures.

A Appendix

A.1 XPS Core Level Fitting Parameters

Fitting of the XPS data, both FlexPes and Bloch, were executed with a fitting algorithm in Igor Pro. The Lorenzian FWHM, Branching ratio and Spin-orbit-split were set to be constant within a core level for both sets of measurements, FlexPES and Bloch.

Table A.1: fit parameters for the In 4d core level from the FlexPES data.

In 4d FlexPES			
	Clean InSb	2nd Bi dep.	3rd Bi dep.
FWHM Lorenz (eV)	0.18	0.18	0.18
Branching ratio	0.79	0.79	0.79
Spin-orbit-split (eV)	0.86	0.86	0.86
B.E. In-Sb bulk (eV)	17.28	17.23	17.21
Intensity In-Sb bulk (a.u.)	0.341	0.424	0.454
FWHM Gauss In-Sb bulk (eV)	0.248	0.302	0.330
B.E. In-Sb surface (eV)	17.50	17.45	17.43
Intensity In-Sb surface (a.u.)	0.186	0.062	0.050
FWHM Gauss In-Sb surface (eV)	0.258	0.198	0.219
B.E. In-Bi (eV)		16.85	16.84
Intensity In-Bi (a.u.)		0.021	0.007
FWHM Gauss In-Bi (eV)		0.291	0.624

Table A.2: fit parameters for the Bi 5d core level from the FlexPES data.

Bi 5d FlexPES		
	2nd Bi dep.	3rd Bi dep.
FWHM Lorenz (eV)	0.21	0.21
Branching ratio	0.84	0.84
Spin-orbit-split (eV)	3.04	3.04
B.E. Bi-Bi, Bi-In (eV)	23.67	23.62
Intensity Bi-Bi, Bi-In (a.u.)	0.556	0.546
FWHM Gauss Bi-Bi, Bi-In (eV)	0.505	0.484
B.E. Bi-Sb (eV)	24.14	24.08
Intensity Bi-Sb (a.u.)	0.245	0.026
FWHM Gauss Bi-Sb (eV)	0.387	0.250

Table A.3: fit parameters for the Sb 4d core level from the Bloch data.

Sb 4d Bloch					
	Clean InSb	1st ann.	2nd ann.	3rd ann.	4th ann.
FWHM Lorenz (eV)	0.23	0.23	0.23	0.23	0.23
Branching ratio	0.80	0.80	0.80	0.80	0.80
Spin-orbit-split (eV)	1.24	1.24	1.24	1.24	1.24
B.E. Sb-In surface (eV)	31.57	31.57	31.57	31.57	31.57
Intensity Sb-In surface (a.u.)	0.224	0.080	0.094	0.124	0.135
FWHM Gauss Sb-In surface (eV)	0.321	0.439	0.358	0.406	0.313
B.E. Sb-In bulk, Sb-Bi (eV)	31.85	31.85	31.85	31.85	31.85
Intensity Sb-In bulk, Sb-Bi (a.u.)	0.416	0.450	0.439	0.425	0.451
FWHM Gauss Sb-In bulk,Sb-Bi (eV)	0.266	0.314	0.289	0.299	0.291

Table A.4: fit parameters for the In 4d core level from the Bloch data.

In 4d Bloch					
	Clean InSb	1st ann.	2nd ann.	3rd ann.	4th ann.
FWHM Lorenz (eV)	0.19	0.19	0.19	0.19	0.19
Branching ratio	0.79	0.79	0.79	0.79	0.79
Spin-orbit-split (eV)	0.86	0.86	0.86	0.86	0.86
B.E. In-Sb bulk (eV)	17.28	17.28	17.28	17.28	17.28
Intensity In-Sb bulk (a.u.)	0.326	0.365	0.355	0.331	0.337
FWHM Gauss In-Sb bulk (eV)	0.241	0.275	0.275	0.233	0.228
B.E. In-Sb surface (eV)	17.50	17.50	17.50	17.50	17.50
Intensity In-Sb surface (a.u.)	0.185	0.098	0.095	0.087	0.070
FWHM Gauss In-Sb surface (a.u.)	0.283	0.303	0.303	0.280	0.244
B.E. In-Bi (eV)		16.99	16.99	16.99	16.99
Intensity In-Bi (a.u.)		0.090	0.093	0.091	0.111
FWHM Gauss In-Bi (eV)		0.282	0.282	0.282	0.322

Table A.5: fit parameters for the Bi 5d core level from the Bloch data.

Bi 5d Bloch				
	1st anneal	2nd anneal	3rd anneal	4th anneal
FWHM Lorenz (eV)	0.20	0.20	0.20	0.20
Branching ratio	0.84	0.84	0.84	0.84
Spin-orbit-split (eV)	3.04	3.04	3.04	3.04
B.E. Bi-Bi, Bi-In (eV)	23.70	23.70	23.70	23.70
Intensity Bi-Bi, Bi-In (a.u.)	0.410	0.460	0.474	0.501
FWHM Bi-Bi, Bi-In (eV)	0.458	0.457	0.459	0.446
B.E. Bi-Sb (eV)	24.17	24.17	24.17	24.17
Intensity Bi-Sb (a.u.)	0.528	0.492	0.457	0.483
FWHM Gauss Bi-Sb (a.u.)	0.553	0.512	0.493	0.446

A.2 XPS Relative Peak Areas of Fits

The relative peak area of the fitted core levels were determined by dividing the fitted peak area with the total area of the core-level-fit minus the background.Hereby, the areas were determined by integrating over the respective peak.

Table A.6: Relative peak area of the fits for the FlexPES data set. Determined from the fitting values of the respective peaks.

FlexPES			
	Clean	2nd dep.	3rd dep.
Bi-Bi, Bi-In	0	0.694	0.954
Bi-Sb	0	0.305	0.046
In-Bi	0	0.041	0.013
In-Sb bulk	0.648	0.837	0.889
In-Sb surface	0.352	0.122	0.098

Table A.7: Relative peak area of the fits for the Bloch data set. Determined from the fitting values of the respective peaks.

BLOCH					
	Clean	1st ann.	2nd ann.	3rd ann.	4th ann.
Bi-Bi, Bi-In	0	0.437	0.483	0.509	0.510
Bi-Sb	0	0.563	0.563	0.491	0.490
In-Bi	0	0.161	0.161	0.163	0.198
In-Sb bulk	0.638	0.661	0.661	0.651	0.651
In-Sb surface	0.362	0.176	0.176	0.171	0.135
Sb-In surface	0.350	0.152	0.152	0.226	0.230
Sb-In, Sb-Bi	0.650	0.848	0.848	0.774	0.770

Bibliography

[1] Leonard J. Brillson. Why Surfaces and Interfaces of Electronic Materials. In *An Essential Guide to Electronic Material Surfaces and Interfaces*, pages 1–13. John Wiley & Sons, Ltd, 2016. Section: 1 _eprint: https://onlinelibrary.wiley.com/doi/pdf/10.1002/9781119027140.ch1.

[2] David Burg and Jesse H. Ausubel. Moore's Law revisited through Intel chip density. *PLOS ONE*, 16(8):e0256245, August 2021. Publisher: Public Library of Science.

[3] R.R. Schaller. Moore's law: past, present and future. *IEEE Spectrum*, 34(6):52–59, June 1997. Conference Name: IEEE Spectrum.

[4] Sandra Benter. *Adventures of III-V Semiconductor Surfaces*. PhD thesis, Lund University, 2023.

[5] Yi Liu. *Surface modification of III-V nanostructures studied by low-temperature scanning tunneling microscopy*. PhD thesis, Lund University, Lund, Sweden, May 2022.

[6] Sudha Mokkapati and Chennupati Jagadish. III-V compound SC for optoelectronic devices. *Materials Today*, 12(4):22–32, April 2009.

[7] Chao Xie, Yi Wang, Zhi-Xiang Zhang, Di Wang, and Lin-Bao Luo. Graphene/Semiconductor Hybrid Heterostructures for Optoelectronic Device Applications. *Nano Today*, 19:41–83, April 2018.

[8] S. Francoeur, M.-J. Seong, A. Mascarenhas, S. Tixier, M. Adamcyk, and T. Tiedje. Band gap of GaAs$_{1-x}$Bi$_x$, 0<x<3.6%. *Applied Physics Letters*, 82(22):3874–3876, June 2003.

[9] Shumin Wang and Pengfei Lu, editors. *Bismuth-Containing Alloys and Nanostructures*, volume 285 of *Springer Series in Materials Science*. Springer Singapore, Singapore, 2019.

[10] Yi Liu, Sandra Benter, Chin Shen Ong, Renan P. Maciel, Linnéa Björk, Austin Irish, Olle Eriksson, Anders Mikkelsen, and Rainer Timm. A 2D Bismuth-Induced Honeycomb Surface Structure on GaAs(111). *ACS Nano*, 17(5):5047–5058, March 2023. Publisher: American Chemical Society.

[11] Yonghu Wang, Shuangying Lei, Neng Wan, Hong Yu, and Jie Chen. Large gap two-dimensional topological insulators with prominent Rashba effect in ethynyl functionalized III-Bi Buckled-Honeycomb monolayers. *Superlattices and Microstructures*, 158:107026, October 2021.

[12] Takuto Nakamura, Yoshiyuki Ohtsubo, Naoki Tokumasu, Patrick Le Fèvre, François Bertran, Shin-ichiro Ideta, Kiyohisa Tanaka, Kenta Kuroda, Koichiro Yaji, Ayumi Harasawa, Shik Shin, Fumio Komori, and Shin-ichi Kimura. Giant Rashba system on a semiconductor substrate with tunable Fermi level: Bi / GaSb (110) − (2 × 1). *Phys. Rev. Materials*, 3(12):126001, December 2019.

[13] M. Z. Hasan and C. L. Kane. Colloquium: Topological insulators. *Rev. Mod. Phys.*, 82(4):3045–3067, November 2010. Publisher: American Physical Society.

[14] Feng-Chuan Chuang, Liang-Zi Yao, Zhi-Quan Huang, Yu-Tzu Liu, Chia-Hsiu Hsu, Tanmoy Das, Hsin Lin, and Arun Bansil. Prediction of Large-Gap Two-Dimensional Topological Insulators Consisting of Bilayers of Group III Elements with Bi. *Nano Lett.*, 14(5):2505–2508, May 2014. Publisher: American Chemical Society.

[15] James McKenzie. Moore's law: further progress will push hard on the boundaries of physics and economics, June 2023.

[16] Del Alamo and Jesús A. Nanometre-scale electronics with III–V compound semiconductors. *Nature*, 479(7373):317–323, November 2011. Publisher: Nature Publishing Group.

[17] M. Ferhat and A. Zaoui. Structural and electronic properties of III-V bismuth compounds. *Phys. Rev. B*, 73(11):115107, March 2006.

[18] X. Lu, D. A. Beaton, R. B. Lewis, T. Tiedje, and M. B. Whitwick. Effect of molecular beam epitaxy growth conditions on the Bi content of GaAs1−xBix. *Applied Physics Letters*, 92(19):192110, May 2008.

[19] Yi Liu, Johan V. Knutsson, Nathaniel Wilson, Elliot Young, Sebastian Lehmann, Kimberly A. Dick, Chris J. Palmstrøm, Anders Mikkelsen, and Rainer Timm. Self-selective formation of ordered 1D and 2D GaBi structures on wurtzite GaAs nanowire surfaces. *Nat Commun*, 12(1):5990, October 2021. Number: 1 Publisher: Nature Publishing Group.

[20] Xiaolong Cheng, Dongjun Li, Yu Jiang, Fangzhi Huang, and Shikuo Li. Advances in Electrochemical Energy Storage over Metallic Bismuth-Based Materials. *Materials*, 17(1):21, January 2024. Number: 1 Publisher: Multidisciplinary Digital Publishing Institute.

[21] Pin-Chun Shen, Cong Su, Yuxuan Lin, Ang-Sheng Chou, Chao-Ching Cheng, Ji-Hoon Park, Ming-Hui Chiu, Ang-Yu Lu, Hao-Ling Tang, Mohammad Mahdi Tavakoli, Gregory Pitner, Xiang Ji, Zhengyang Cai, Nannan Mao, Jiangtao Wang, Vincent Tung, Ju Li, Jeffrey Bokor, Alex Zettl, Chih-I Wu, Tomás Palacios, Lain-Jong Li, and Jing Kong. Ultralow contact resistance between semimetal and monolayer semiconductors. *Nature*, 593(7858):211–217, May 2021.

[22] Shengpeng Huang. Characterization of Bi-incorporated InSb(111)A/B Surfaces. Master's thesis, Lund University, 2023.

[23] Sandra Benter, Yi Liu, Renan Da Paixao Maciel, Chin Shen Ong, Lassi Linnala, Dong Pan, Austin Irish, Yen-Po Liu, Jianhua Zhao, Hongqi Xu, Olle Eriksson, Rainer Timm, and Anders Mikkelsen. Tuneable 2D surface Bismuth incorporation on InAs nanosheets. *Nanoscale*, 15(21):9551–9559, June 2023. Publisher: The Royal Society of Chemistry.

[24] Ernst Meyer, Roland Bennewitz, and Hans J. Hug. *Scanning Probe Microscopy: The Lab on a Tip*. Graduate Texts in Physics. Springer International Publishing, Cham, 2021.

[25] Peter Sutter. Scanning Tunneling Microscopy in Surface Science. In Peter W. Hawkes and John C. H. Spence, editors, *Springer Handbook of Microscopy*, pages 1331–1368. Springer International Publishing, Cham, 2019. Series Title: Springer Handbooks.

[26] Prof. Dr. Stefan Kümmel. Quantummechanik I. University of Bayreuth, Bayreuth, Germany, 2019.

[27] J. Bardeen. Tunnelling from a Many-Particle Point of View. *Phys. Rev. Lett.*, 6(2):57–59, January 1961.

[28] J. Tersoff and D. R. Hamann. Theory of the scanning tunneling microscope. *Phys. Rev. B*, 31(2):805–813, January 1985.

[29] Jagdish Kumar. Photoelectron Spectroscopy: Fundamental Principles and Applications. In Surender Kumar Sharma, editor, *Handbook of Materials Characterization*, pages 435–495. Springer International Publishing, Cham, 2018.

[30] George H. Major, Neal Fairley, Peter M. A. Sherwood, Matthew R. Linford, Jeff Terry, Vincent Fernandez, and Kateryna Artyushkova. Practical guide for curve fitting in x-ray photoelectron spectroscopy. *Journal of Vacuum Science & Technology A*, 38(6):061203, December 2020.

[31] Giulio D'Acunto. *Reaction Mechanisms and Dynamics in the Early Stage of High-κ Oxide Atomic Layer Deposition*. PhD thesis, Lund, 2022.

[32] Fred A. Stevie and Carrie L. Donley. Introduction to x-ray photoelectron spectroscopy. *Journal of Vacuum Science & Technology A: Vacuum, Surfaces, and Films*, 38(6):063204, December 2020.

[33] Pardis Simon, Víctor G. Baldovino-Medrano, and Robert Wojcieszak. X-Ray Photoelectron Spectroscopy (XPS): Principles and Application for the Analysis of Photoactive Materials. In Detlef Bahnemann and Antonio Otavio T. Patrocinio, editors, *Springer Handbook of Inorganic Photochemistry*, pages 249–271. Springer International Publishing, Cham, 2022.

[34] C. Julian Chen. *Introduction to Scanning Tunneling Microscopy*. Oxford University Press, March 2021.

[35] M. P. Seah and W. A. Dench. Quantitative electron spectroscopy of surfaces: A standard data base for electron inelastic mean free paths in solids. *Surface and Interface Analysis*, 1(1):2–11, 1979. _eprint: https://onlinelibrary.wiley.com/doi/pdf/10.1002/sia.740010103.

[36] Katariina Pussi and Renee D. Diehl. Low-Energy Electron Diffraction. In *Characterization of Materials*, pages 1–15. John Wiley & Sons, Ltd, 2012. _eprint: https://onlinelibrary.wiley.com/doi/pdf/10.1002/0471266965.com085.pub2.

[37] Kurt W. Kolasinski. Surface and Adsorbate Structure. In *Surface Science: Founrdations of Catalysis and Nanoscience*, pages 9–49. John Wiley & Sons, Ltd, 2012. Section: 1 _eprint: https://onlinelibrary.wiley.com/doi/pdf/10.1002/9781119941798.ch1.

[38] Lyudmila V Goncharova. *Basic Surfaces and their Analysis:*. Morgan & Claypool Publishers, June 2018.

[39] Sadao Adachi. Indium Antimonide (InSb). In Sadao Adachi, editor, *Optical Constants of Crystalline and Amorphous Semiconductors: Numerical Data and Graphical Information*, pages 268–278. Springer US, Boston, MA, 1999.

[40] I. Vurgaftman, J. R. Meyer, and L. R. Ram-Mohan. Band parameters for III–V compound semiconductors and their alloys. *Journal of Applied Physics*, 89(11):5815–5875, June 2001.

[41] Kristin A. Persson. Materials Data on InSb by Materials Project, 2020.

[42] K. Momma and F. Izumi. VESTA 3 for three-dimensional visualization of crystal, volumetric and morphology data. *J Appl Cryst*, 44(6):1272–1276, December 2011. Publisher: International Union of Crystallography.

[43] Andrea Troian. *Synchrotron X-ray based characterization of technologically relevant III-IV surfaces and nanostructures*. PhD thesis, Division of Synchrotron Radiation Research, Department of Physics, Lund University, Lund, 2019.

[44] Settimio Mobilio, Federico Boscherini, and Carlo Meneghini, editors. *Synchrotron Radiation: Basics, Methods and Applications*. Springer, Berlin, Heidelberg, 2015.

[45] Pedro F. Tavares, Simon C. Leemann, Magnus Sjöström, and Ake Andersson. The MAX IV storage ring project. *J Synchrotron Radiat*, 21(Pt 5):862–877, September 2014.

[46] Alexei Preobrajenski, Alexander Generalov, Gunnar Öhrwall, Maxim Tchaplyguine, Hamed Tarawneh, Stephan Appelfeller, Eleanor Frampton, and Noelle Walsh. FlexPES: a versatile soft X-ray beamline at MAX IV Laboratory. *J Synchrotron Rad*, 30(4):831–840, July 2023.

[47] The FlexPES beamline team. MAX IV Beamline review Report: FlexPES, September 2022.

[48] The Bloch beamline team. Beamline review Report BLOCH, April 2022.

[49] Dr. Eberl MBE-Komponenten GmbH. Low Temperature Effusion Cell NTEZ 40-10-22-S-2107249 Operation Instructions.

[50] Maria Grazia Betti, Davide Berselli, and Carlo Mariani. Electronic properties of (lxn)-reconstructed Bi/lnSb(ll0) interfaces. *Journal of Electron Spectroscopy and Related Phenomena*, 76:465–469, December 1995.

[51] P. J. Kowalczyk, O. Mahapatra, D. N. McCarthy, W. Kozlowski, Z. Klusek, and S. A. Brown. STM and XPS investigations of bismuth islands on HOPG. *Surface Science*, 605(7):659–667, April 2011.

[52] Fausto Calderazzo. Synthesis and Crystal and Molecular Structure of Tetraphenyldibismuthine, Bi2Ph4,the First Crystallographically Characterized Tet raorganyl Derivative of Bismuth(l1). *J. Chem. Soc., Chem. Commun.*, 1983.

[53] Andreas Kuczkowski, Stefan Heimann, Anna Weber, Stephan Schulz, Dieter Bläser, and Christoph Wölper. Structural Characterization of Et4Sb2 and Et4Bi2. *Organometallics*, 30(17):4730–4735, September 2011. Publisher: American Chemical Society.

[54] M.C. Richter, J.-M. Mariot, M.A. Gafoor, L. Nicolaï, O. Heckmann, U. Djukic, W. Ndiaye, I. Vobornik, J. Fujii, N. Barrett, V. Feyer, C.M. Schneider, and K. Hricovini. Bi atoms mobility-driven circular domains at the Bi/InAs(111) interface. *Surface Science*, 651:147–153, September 2016.

[55] Sandra Benter, Yi Liu, Renan Da Paixao Maciel, Chin Shen Ong, Lassi Linnala, Dong Pan, Austin Irish, Yen-Po Liu, Jianhua Zhao, Hongqi Xu, Olle Eriksson, Rainer Timm, and Anders Mikkelsen. Tuneable 2D surface BIsmuth incorporation on InAs nansheets-Supplementary files. *Nanoscale*, 15(21), June 2023.

[56] T. van Gemmeren, L. Lottermoser, G. Falkenberg, L. Seehofer, R. L. Johnson, L. Gavioli, C. Mariani, R. Feidenhans'l, E. Landemark, D. Smilgies, and M. Nielsen. Bismuth-induced restructuring of the GaSb(110) surface. *Phys. Rev. B*, 57(7):3749–3752, February 1998. Publisher: American Physical Society.

[57] P. W. Hawkes and John C. H. Spence, editors. *Science of microscopy*. Springer, New York, 2007. OCLC: ocm62796281.

[58] Yaxin Zhai, Sangita Baniya, Chuang Zhang, Junwen Li, Paul Haney, Chuan-Xiang Sheng, Eitan Ehrenfreund, and Zeev Valy Vardeny. Giant Rashba splitting in 2D organic-inorganic halide perovskites measured by transient spectroscopies. *Science Advances*, 3(7):e1700704, July 2017. Publisher: American Association for the Advancement of Science.

[59] Frank Ortmann, Stephan Roche, and Sergio O. Valenzuela. *Topological insulators: fundamentals and perspectives*. Wiley-VCH Verlag GmbH & Co. KGaA, Weinheim, Germany, 1st. edition edition, 2015.

Acknowledgements